Wall shear stress characteristics of a turbulent boundary layer obtained with multi-aperture defocusing μPTV and high-speed stereo profile-PIV

J. Klinner[1,*], C. Willert[1]

1: DLR Institute of Propulsion Technology, German Aerospace Center, Germany
*Corresponding author: joachim.klinner@dlr.de

Keywords: fluid flow measurement, turbulent boundary layer, wall shear stress, spanwise fluctuations, multi-aperture, defocusing, particle tracking, PTV.

ABSTRACT

A multi-aperture 3d 3c micro PTV system is presented which relies on single window optical access for both high-speed tracer illumination and image recording. Similar to the "defocusing" concept described by C. Willert & Gharib (1992), the wall distance of individual particles is obtained from the size of projected particle image triplets formed by a triplet of apertures on the entrance pupil of the microscope lens. The present article extends upon previously published material (Klinner & Willert, 2022) by applying the technique on a canonical turbulent boundary layer (TBL) to track the near-wall motion of tracer particles with the aim of estimating the unsteady wall-shear stress from particle tracks. The technique is validated with measurements of a TBL inside the closed test section of the 1 m wind tunnel of DLR in Göttingen (1mWK) at free- stream velocities of $5.2 \leq U_\infty \leq 20\,\mathrm{m/s}$ with corresponding shear Reynolds numbers of $560 \leq \mathrm{Re}_\tau \leq 1630$. In the viscous sublayer, the joint probability density distributions of stream- and spanwise wall shear stress (WSS) components could be reliably captured down to probability densities of 10^{-3}. As far as we know, this has not been achieved in the past, particularly not for the spanwise component. For the streamwise component the measured Reynolds-number dependency of $\tau_{x,\mathrm{rms}}$ agrees to correlations by Örlü & Schlatter (2011). Furthermore, the skewness of the streamwise WSS S_{τ_x} agrees well to values from DNS. On the other hand, the spanwise fluctuations $\tau_{z,\mathrm{rms}}$ consistently underestimate the predicted DNS values, for which it is assumed that the deviation can be explained by the rapid decrease of the spanwise fluctuations w_{rms}/U with increasing wall distance. Wall-normal profiles of 3c velocity statistics were obtained by bin averaging of particle velocities. Up into the buffer layer, these profiles are consistent with profiles from stereo PIV as well as from DNS and LES, indicating an accurate determination of both near-wall velocities and inner scaling.

1. Introduction

Measurement techniques capable of measuring the 3c fluctuating wall shear stress on submerged bodies are of great importance to improve the physical understanding of wall-bounded turbulent flows, the details of flow separation, the mechanisms governing viscous drag and convective heat

transfer and structural vibrations in several engineering applications including aviation, shipping and road transportation. In general, the viscous skin friction is related to the streamwise and spanwise characteristics of the wall-shear stress $\vec{\tau}_w$ and can be estimated from tracer particle's velocity $\mathbf{u}$ through the relation:

$$\vec{\tau}_w = \mu \left. \frac{\partial \mathbf{u}}{\partial y} \right|_{y=0} \approx \mu \frac{\mathbf{u}(\Delta y)}{\Delta y} \tag{1}$$

with μ representing the dynamic viscosity. Linearity between wall-shear stress and fluid velocity can be assumed within 2% deviation for wall distances $y^+ \leq 4$ (see Fig. 1). Here the superscript $(+)$ denotes viscous scaling where the length unit is defined as $l^* = \nu/u_\tau$, with ν being the kinematic viscosity and $u_\tau = \sqrt{\overline{\tau}/\rho}$ the friction velocity of the boundary layer flow. In particular, l^* and u_τ are essential scaling parameters of mean and fluctuating velocity profiles in TBL. With respect to the organization of near-wall structures of turbulent wall-bounded flows and its interaction with the larger structures from the outer layer, the positive skewed streamwise wall shear stress distribution and its so-called near-wall events, i.e. *reverse flow events* or *extreme positive events*, have received increased attention as they are indicators of the high intermittency of the wall shear stress, which in turn has impact on the mixed scaling in the wall-attached eddies range when modeling wall-bounded flows (Diaz-Daniel et al., 2017; Cardesa et al., 2019). In recent years, numerical simulations at moderate Reynolds numbers indicate a Reynolds-number dependency of the streamwise and spanwise wall shear stress which is rather important for the physical understanding of the mixed scaling of inner and outer units (Hu et al., 2006; Örlü & Schlatter, 2011).

On the other hand, the experimental database with regard to WSS fluctuations and their Reynolds number dependency is very limited, especially with regard to the spanwise component (Diaz-Daniel et al., 2017; Örlü & Vinuesa, 2020). In the case of particle-based velocimetry, this is due to the fact that an accurate estimation of the WSS relies on accurate measurement of two quantities, namely, the instantaneous near-wall velocity within the viscous sublayer ($y^+ < 5$) along

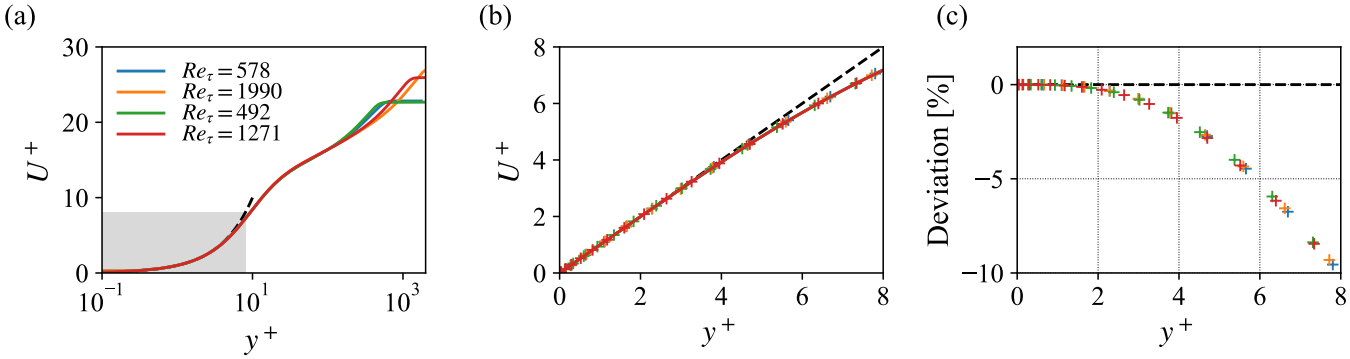

Figure 1. Mean streamwise velocity profiles from DNS of TBLs by Simens et al. (2009) and Schlatter & Örlü (2010a) in log-scaling (a), linear scaling in near the wall (b) and deviation of velocity U^+ from linearity (c).

with the distance from the wall at which the velocity measurement is obtained. For many laser-based techniques this is very challenging due to laser light reflections limited in the vicinity of the wall. Spatial resolution issues impose limitations on capturing strong gradients in the flow. Finally many single-camera particle velocimetry techniques rely on imaging configurations that restrict the measurement to at most two components which generally leaves the spanwise motions unaccounted for.

HS-PIV at high image magnification has recently been shown capable of providing instantaneous streamwise wall shear in a zero pressure gradient (ZPG) TBL at Re_τ up to 5600 ($u_\tau = 0.34\mathrm{m\,s^{-1}}$) by fitting the unsteady velocity gradient $\partial u/\partial y$ derived from 1d cross-correlation of wall-parallel image rows (C. Willert, 2015; C. E. Willert et al., 2018). Beyond mean and fluctuating velocity profiles, which coincide with direct numerical simulation (DNS) calculations, the resulting probability density distributions of wall shear indicated occasional reverse flow events, which were confirmed by searching for near-wall velocities in the time traces. Although the streamwise and wall-normal extents of reverse flow regions correspond to DNS by Lenaers et al. (2011), the spanwise extent of these structures remain uncovered and requires more complex 3d-3c imaging techniques.

On the other hand, reduced seeding densities in the viscous sublayer opens up new possibilities for 3d particle tracking velocimetry (PTV), which allows the capture of both components of the WSS vector. Defocusing micro particle tracking velocimetry (μPTV) (Fuchs & Kähler, 2019) along with astigmatism μPTV (Chen et al., 2009; Cierpka et al., 2010; Barnkob & Rossi, 2020) and digital holographic methods (Sheng et al., 2008) have the potential of providing time-resolved 3d-3c velocity data and feature a relatively low hardware complexity using a single high-speed camera and a combined optical access for both tracer illumination and imaging. Fuchs et al. (2023) applied defocusing μPTV in the viscous sublayer of a ZPG TBL at Re_τ up to 8940 with $u_\tau = 1.37\mathrm{m\,s^{-1}}$ and evaluated mean and fluctuating velocities up to wall distances of $y^+ = 6$. While mean axial velocities agreed well with the linear region in the viscous sub layer up to Re_τ 3260 ($u_\tau = 0.46\mathrm{m\,s^{-1}}$), with increasing Re_τ slight underestimation of mean velocities was observed. Diagnostics plots indicated overestimation of fluctuating velocities near the wall. The authors concluded, that defocusing μPTV is a feasible concept for the measurement of the mean wall shear but suffers from increasing uncertainties of particle positions with increasing wall distance.

Kumar et al. (2021) chose to use a single-axis holographic arrangement to image particles in liquid flow using digital fresnel reflection holography (DFRH). With this setup the authors were able to capture particle tracks in a volume with stream and spanwise extends of $20\,l^*$ and a wall normal extend of from $0.1 < y^+ \leq 12$ in a turbulent channel flow at Re_τ=400. Noticeably, the authors recorded several tracks with strongly meandering motion and increased acceleration in the viscous sublayer with spans of $2 - 3\,l^*$ stating, that to date, there are hardly any experimental studies that allow a quantification of these near-wall spanwise motions by non-intrusive measurements. Probability density distributions achieved good agreement with DNS predictions in the range $\tau_x^+ \leq$

2 and $-1 \leq \tau_z^+ \leq 1$ with deviations toward the extreme ends, e.g. rare reverse flow events and high stress events were underestimated. The authors suspected that the deviations from DNS are caused by resolution issues that lead to an underestimation of streamwise high stress events and an overestimation of the spanwise stress events.

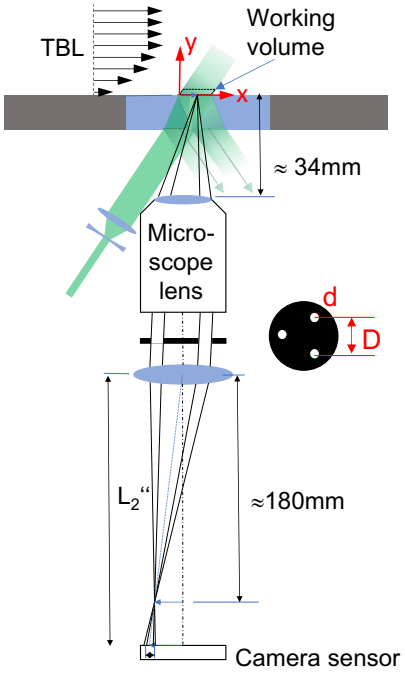

Figure 2. Optical arrangement for MA-μPTV for boundary layer measurements using single window access.

In the following we will present a measurement system based on 3d-3c micro PTV that is capable of simultaneously providing unsteady measurements of both the streamwise as well as spanwise components of the wall shear stress (WSS) vector. The instrument is based on a single high-speed camera and a microscope lens along with a high-speed laser (Fig. 2) for particle illumination. Within the microscope lens a mask with a triplet of apertures implements a depth-from-defocus concept as initially introduced by C. Willert & Gharib (1992), a concept that is also known as *aperture encoded imaging*. The depth encoding is based on the separation of multiple images of the same particle, generated by different – in this case three – beam paths through a pinhole mask placed in the lens pupil. In the following, these self-similar particle image triplets will be referred to as *triplets*. To avoid confusion with *defocusing* μPTV the term MA-μPTV is used to describe the imaging setup used herein.

Since its introduction by C. Willert & Gharib (1992), the "defocusing concept" shifted toward the use of multiple cameras for applications at macroscopic scale to avoid increased crowding of the detector at higher particle densities and to increase the depth sensitivity by increasing the separation of the individual "apertures" (see e.g. Pereira et al., 2000; Pereira & Gharib, 2002). On the other hand, single lens configurations typically have been used in microscopic imaging applications (Yoon & Kim, 2006; Pereira et al., 2007; Lu et al., 2008). Pereira et al. (2000) and Pereira & Gharib (2002) applied the multi-aperture defocusing concept in two-phase macroscopic flows

and extended the imaging model to multiple cameras not only to eliminate the problem of image crowding by triplets but to increase the depth resolution. The authors derived equations describing the optical geometry and to enable error estimates for the particle locations.

Returning to the single camera approach and using the simplified geometric analysis as provided in C. Willert & Gharib (1992) and Pereira & Gharib (2002), the depth sensitivity of a microscopic setup can be predicted for different pinhole separations. For example, for a typical long working distance microscope objective with magnification of $5\times$ and at a typical pixel pitch for high-speed cameras of $13.5\,\mu\mathrm{m}$, a nearly constant sensitivity of $83\,\mathrm{pixel\,mm^{-1}}$ can be achieved for a measurement volume of 0.5 mm depth if the pinhole spacing fully utilizes the diameter of the entrance pupil. Assuming that the triplet size can be detected with sub-pixel accuracy of 0.5 pixel, such a sensitivity would be sufficient to achieve an accuracy in y of $6\,\mu\mathrm{m}$, which we found promising. Another aspect is that small pinhole diameters result in a reduced beam divergence compared to defocusing PTV, and thus to a lower particle image broadening over depth, albeit at proportionally reduced particle image intensities.

Yoon & Kim (2006) applied the multiple pinhole technique in microfluidics using a microscopic objective with $m = 20$ and pinholes with $1.5\,\mathrm{mm}$ diameter. Cierpka et al. (2010) has estimated the ratio of peak image intensity to noise floor to be one order of magnitude lower for MA-µPTV in comparison to astigmatism µPTV for such a imaging configuration. On the other hand, using this microscopic setup Yoon & Kim (2006) have successfully applied MA-µPTV to a backward facing step and quantified the root mean square (RMS) of the depth position to be in the order of $0.2\,\mathrm{pixel}$ at a depth sensitivity of $1.2\,\mu\mathrm{m\,pixel^{-1}}$. Also, the authors observed a non-linearity of the depth sensitivity and observed that each vertex of the triangular image pattern increases at different rate with depth and image position, which originates from deviations from self-similarities of triplet images, even though the three pinholes are arranged equilateral. The authors compensated for this non-linearity by applying polynomial calibration functions that depend on the image coordinates and also introduced a similarity parameter to distinguish overlapping particle images.

In our previous work, the feasibility of MA-µPTV for WSS measurements was demonstrated in a developing turbulent duct flow of a small wind tunnel up to Re_τ=836 (Klinner & Willert, 2022). The present contribution extends upon previously published material by applying MA-µPTV on a well-characterized TBL to track the near-wall motion of tracer particles with the aim of estimating the unsteady wall-shear stress from the particles' velocity and comparing the data with DNS results from literature.

2. Measurement setup

2.1. MA-μPTV system

All measurements are performed on the closed test section of the 1 m wind tunnel of DLR in Göttingen (1mWK) at free-stream velocities of $5.2\,\mathrm{m/s} \leq u_{\mathrm{bulk}} \leq 20\,\mathrm{m/s}$ and corresponding shear Reynolds number $560 \leq \mathrm{Re}_\tau \leq 1630$ and friction velocities $0.22\,\mathrm{m/s} \leq u_\tau \leq 0.74\,\mathrm{m/s}$. As shown in Fig. 3a, the high-speed camera (Vision Research V2640) and an infinity corrected microscope lens (Mitotuyo Plan Apo 5×, $f = 40\,\mathrm{mm}$) are placed below the test section. Since the measurement volume is imaged directly through the glass wall, issues that would normally arise with side-viewing configurations such as parallax and perspective errors due to the slight oblique viewing angle (Cierpka et al., 2013) are mitigated here.

The microscope objective is combined with a microscope tube lens of $f = 180\,\mathrm{mm}$ which results in an effective magnification of $4.5\times$. The pinhole mask consists of a black anodized aluminum foil which is located in the nearly parallel optical path between the objective and the tube lens (cf. Fig. 2). The mask contains three precision-milled pinholes each with a diameter $2\,\mathrm{mm}$ that form an equilateral triangle. The spacing between the pinholes D is maximized such that the apertures fall just inside the entrance pupil diameter $D_{ep} = 11.2\,\mathrm{mm}$ of the objective.

The collimated beam from two high-speed pulsed lasers (2× Innolas Photonics Nanio Air) is introduced at an angle of about 30° through the same flush-mounted window in the wind tunnel wall. Both lasers have an average power of $10\,\mathrm{W}$ at a pulse repetition rate of $40\,\mathrm{kHz}$. A beam expander is used to increase the beam diameter to roughly $2.0\,\mathrm{mm}$ to enable illumination of the entire measurement volume (cf. Fig. 3). The oblique laser incidence was chosen to prevent direct back reflections of the laser light from the window into the objective, thus reducing the risk of damage to the camera sensor.

Within the wind tunnel the TBL is tripped about $1.5\,\mathrm{m}$ upstream of the measurement location allowing it to grow to a thickness of about $35\,\mathrm{mm}$ at the measurement location. The flow is seeded with $1-2\,\mu\mathrm{m}$ aerosol droplets from a water-based fog generator. To match the free-stream velocity, the frame rate of the high-speed camera is varied between $20\,\mathrm{kHz}$ and $37\,\mathrm{kHz}$ with a field of view of 640×480 pixel or 768×360 pixel in streamwise and spanwise directions, respectively. Per condition up to 16 sequences of 39 000 to 51 000 images constitute the basis for the subsequent 3D-PTV processing. Table 1 provides an overview on test points for which sequences were acquired with MA-μPTV and high-speed profile PIV.

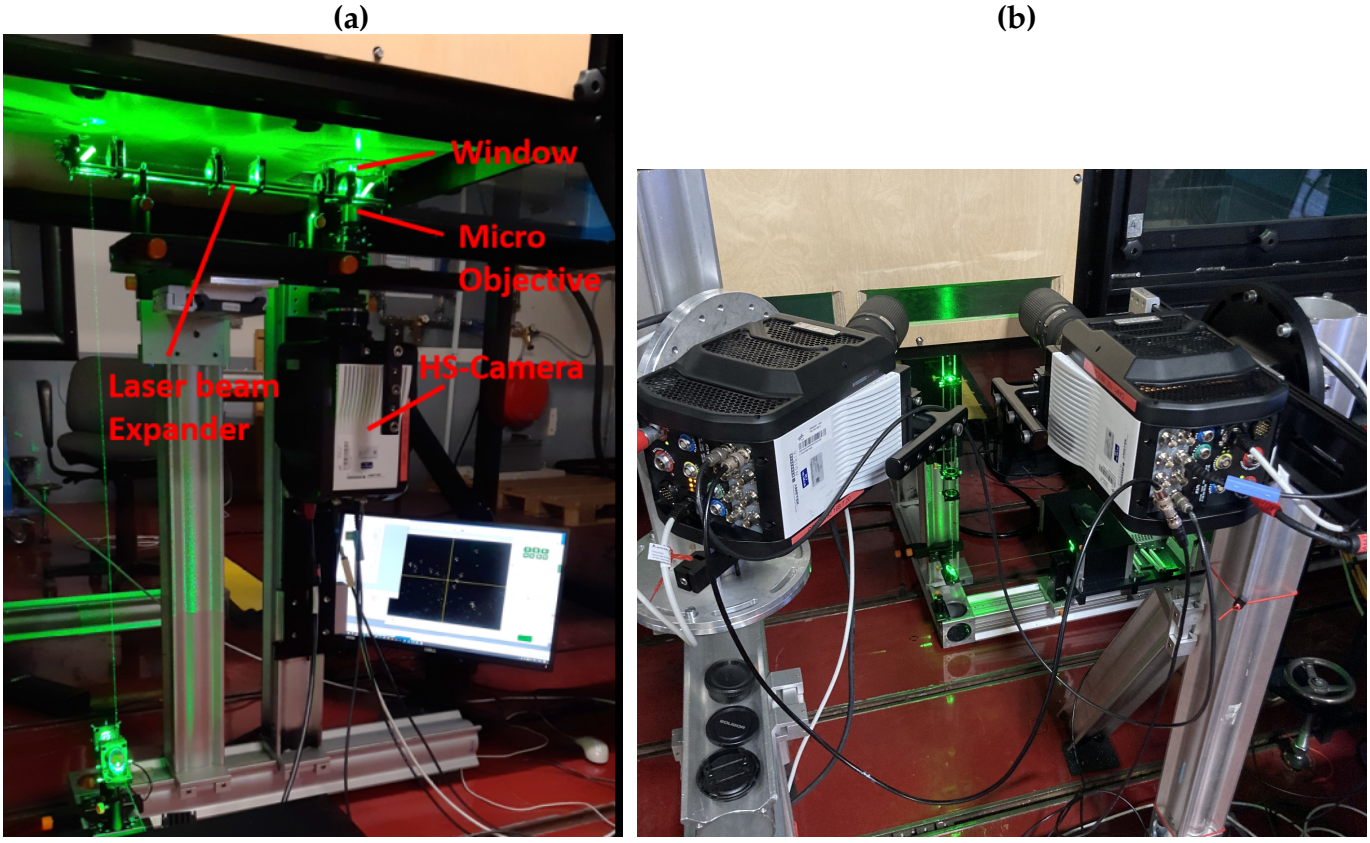

Figure 3. (a) Photograph of the optical setup for measurements at the one-meter low-speed wind tunnel at the DLR Göttingen (b) camera setup for stereoscopic high-speed profile PIV measurements.

2.2. Profile PIV reference measurements

Comparative measurements of the TBL are provided through high-speed profile PIV (C. Willert, 2015) which also provides accurate estimates of the outer BL parameters as edge velocity, BL thickness, momentum and displacement thickness along with the corresponding Reynolds numbers in Tab. 1. For these measurements a field of view (FOV) of $4.0\,\mathrm{mm} \times 51.2\,\mathrm{mm}$ (160×2048) captured the complete boundary layer height at camera framing rates of $10\,\mathrm{kHz}$ to $40\,\mathrm{kHz}$. For each free stream velocity, 8 records of 38 000 images were obtained and processed using a triple-frame cross-

Table 1. Overview on the experimental dataset acquired at the 1mWK at the DLR Göttingen.

u_{bulk} [m/s]	u_e [m/s]	δ_{99} [mm]	u_τ [m/s]	l^* [µm]	Re_τ	Re_θ	f_s [kHz]	Samples $n_r \times n_s$	Image size MA-µPTV [Pixels]	[mm^2]
5.2	5.25	38.75	0.223	69	563	1573	20	8×38 888	640×480	1.86×1.40
5.2	5.25	38.75	0.223	69	563	1572	28	8×38 888	640×480	1.86×1.40
7.5	7.57	38.12	0.304	51	754	2265	28	16×38 888	640×480	1.86×1.40
10.0	10.17	36.84	0.390	39	934	2895	28	16×51 372	640×360	1.86×1.05
15.0	15.21	34.50	0.560	28	1251	4009	37	16×51 372	640×360	1.86×1.05
20.0	20.29	34.37	0.736	21	1630	5227	37	16×45 228	768×360	2.23×1.05

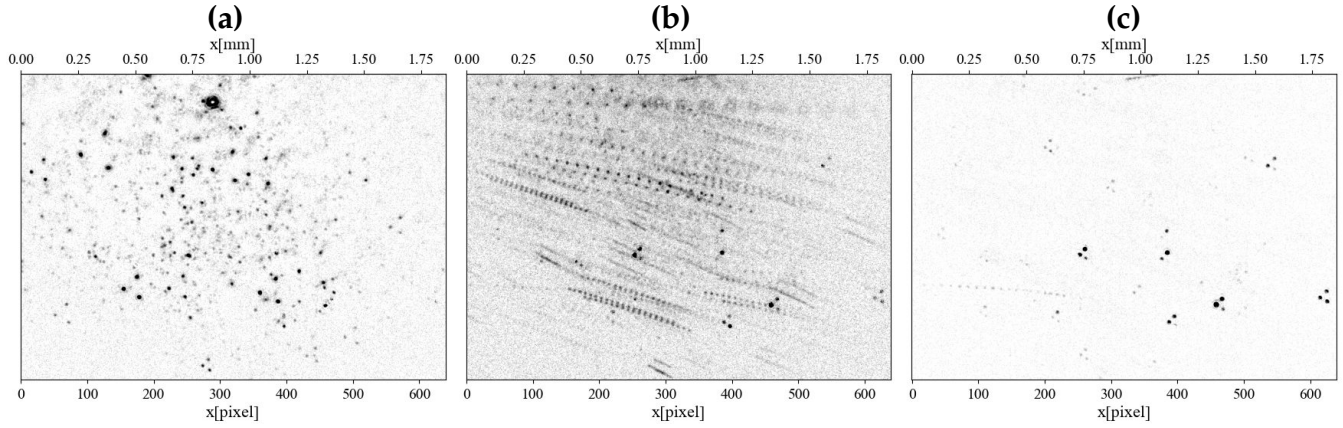

Figure 4. (a) MA-µPTV sample image recorded in the turbulent boundary layer at $\mathrm{Re}_\tau = 754$ (b) Composite image showing particle tracks obtained by overlaying 20 successive recordings acquired at $28\,\mathrm{kHz}$ (c) minimum image showing only stationary particles (mean flow is from left to right).

correlation based algorithm.

In a second set of measurements the 2d-2c HS-PIV setup is extended with a second camera to provide stereoscopic 2d-3c data of the flow field thereby allowing for the recovery of the spanwise velocity component w (see Fig. 3(b)). Magnification is increased by $50\,\%$ to provide a reduced FOV of $2.5\,\mathrm{mm} \times 32.5\,\mathrm{mm}$ at about $16\,\mu\mathrm{m}/\,\mathrm{pixel}$. At the lowest velocity of $u_{\mathrm{bulk}} = 5.2\ \mathrm{m/s}$ this corresponds to about 4.3 pixel/l^* reducing to 1.3 pixel/l^* at $u_{\mathrm{bulk}} = 20\ \mathrm{m/s}$. When processed with samples of 48×6 pixel, effects due to spatial smoothing arise that in particular attenuate estimates of the velocity variances with increasing velocities (C. Willert et al., 2021) and prevent reliable measurements in single viscous unit range.

3. Triplet image characteristics and calibration

Fig. 4 highlights some peculiarities of recorded triplet images. Compared to profile PIV, the images are relatively sparsely populated with particles due to the relatively small extent in the direction of flow of 1.8 mm with a magnification that is $4 - 5\times$ larger in comparison to PIV. Strong gradients in the BL may also lead to an inertia-induced reduction in the number of particles within the viscous sublayer. The reduced particle image density in fact is beneficial for PTV as it improves the triplet matching probability.

Inspecting Fig. 4(a) it can be observed that at a given wall distance particle images exhibit very different brightness levels. Reason for this are the varying scattering behavior of tracer particles of differing sizes as well as differences in irradiance in the obliquely incident Gaussian laser beams. In addition, the vertices of a single triplet can vary in brightness and width due to the inhomogeneous scattering behavior of the liquid droplets combined with the coherent nature of the laser light source (Mie scattering). The defocused particle images have relatively large diameters of around

six pixels, with the width varying only slightly within $0.8\,\mathrm{mm}$ depth of field. Since the pinhole mask blocks most of the light back-scattered by the tracers, particle image intensities are sometimes just above the background level.

To obtain the triangular shape and orientation at various depth positions a calibration procedure was conducted using a lithographically manufactured dot grid on a glass substrate with the glass surface aligned parallel with the bottom wall of the windtunnel. The dot diameter was $5\,\mu\mathrm{m}$ at an equilateral spacing of $150\,\mu\mathrm{m}$ along x and y. The glass plate was back-lit with a green LED and was traversed by a small motorized translation stage. The translation stage was driven by a piezo motor in closed loop operation with position feedback by a linear encoder (accuracy of $0.2\,\mu\mathrm{m}$).

Fig. 5 shows composite images of calibration images of triplets in different image corners at different wall distances y. Dot image centers were obtained by a 2d Gaussian fit. With respect to a reference triangle $\vec{e}_1,\ \vec{e}_2,\ \vec{e}_3$ determined at the measurement volumes center, in each image corner the triplets $\vec{a}_1,\ \vec{a}_2,\ \vec{a}_3$ not only vary in size but also are slightly skewed and deviate from self-similarity with respect to the reference triangle. To emphasize this point, the maximum angular deviation with respect to the three sides are also provided in the plot. Although the pinholes were arranged as equilateral triangles, the reference triplet (cf. Fig. 5, center) already exhibits different side lengths. Also, Fig. 5 indicates, that the particle's positions by triangles centroids (i.e. the mean of vertices) does not coincide involving displacements over y of $1.74 - 3.7\,\mathrm{pixel/mm}$. Applying Yoon and Kim's definition of particle position using the circumcenter of the triangle led to slightly higher scattering of deviations in the range $1.47 - 5.07\,\mathrm{pixel/mm}$.

Deviations of the triplet images from an equilateral pinhole shape were already observed by Yoon & Kim (2006). As possible causes the authors suggested imperfections of the pinhole mask and its de-centering with respect to the lens. In the present experiment, it was also observed that the de-centering between the rigid tube system – consisting of microscope lens, pinhole mask and tube lens – and the camera sensor also is a significant factor. This de-centering was compensated as best as possible by translating the tube lens system laterally to the sensor. Remaining imperfections and triplet distortions were compensated using a set of calibration parameters that will be described in the following.

To quantify deviations from self-similarity and to assign triplet images from neighboring dot images we use the similarity parameter S, defined as:

$$S = Min\left\{\frac{\vec{a}_i \cdot \vec{e}_i}{\|\vec{a}_i\|\,\|\vec{e}_i\|}\right\}_{i=1,2,3} \tag{2}$$

Figure 6(a) indicates the range of S of triplet images in different image regions when at each node the triplet nearest to the wall serves as reference. The deviations in S are evident because the direction of the sides $\vec{e}_1,\ \vec{e}_2,\ \vec{e}_3$ is not constant, as illustrated in Fig. 6(b) for $\vec{e}_1$. It can be observed that the direction varies non-linearly with both the image position and the wall distance, which is demonstrated by the second order polynomial fit.

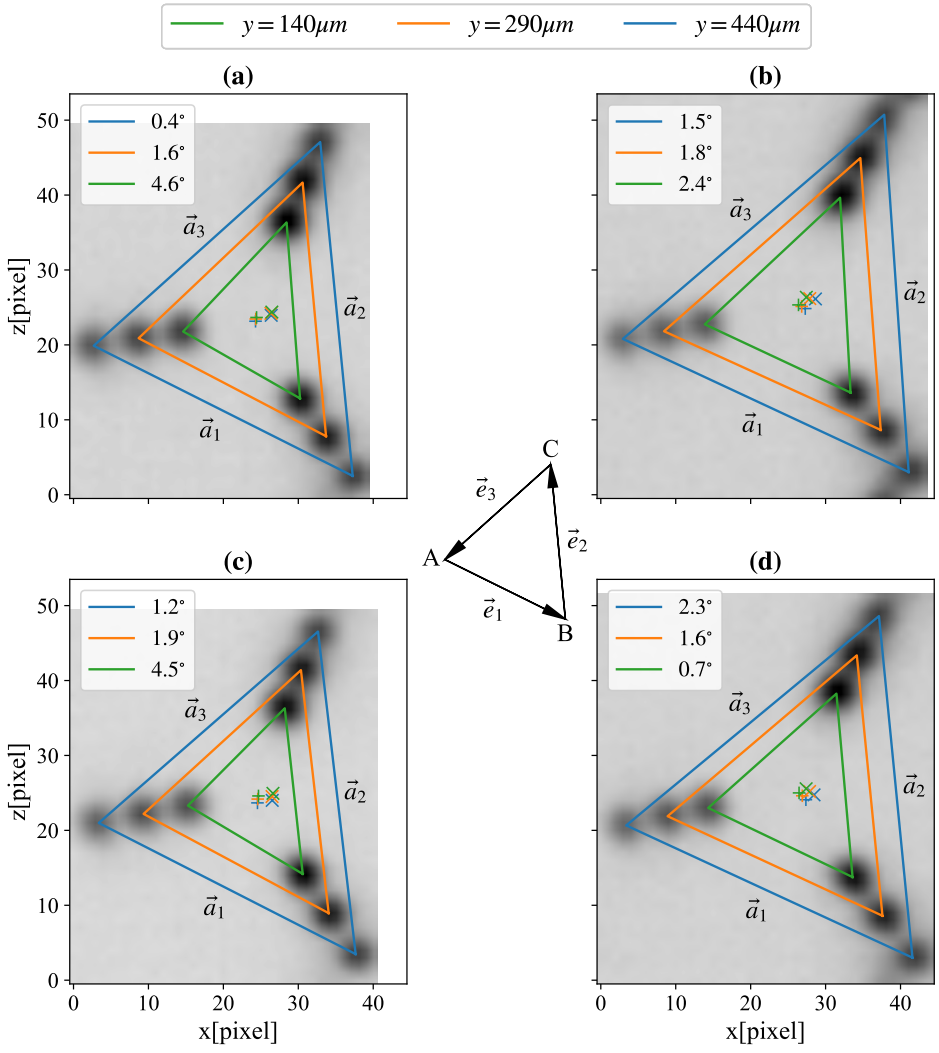

Figure 5. Composite images of calibration images taken at different wall distances z and at the (a) top left (b) top right (c) bottom left (d) bottom right image corners including the maximum angular deviations from reference triangle sides; $+$: particle position by a center of mass; $\times$: particle position by center of the circumcircle.

Since the matching of particle images belonging to the same triplet is based on both certain similarity thresholds with respect to reference triplets $\vec{e}_1$, $\vec{e}_2$, $\vec{e}_3$ and the position estimates x, y, z, these reference vectors are finally obtained from a second order polynomial over y for which the three parameters are linearly interpolated over x and z. In total 9 parameters are used. The resulting curves are shown by the dashed lines which are biased with largest deviations on the top right and bottom left image corner. These deviations were found to be acceptable within the tolerated similarity of $S > 0.998$.

Figure 6(c) indicates a constant slope of the separation gradient $\partial b_{AB}/\partial y$ which increases proportionally with the depth position but exhibits a varying offset between $18 - 22$ pixels corresponding to an offset of about $y_0 = 190\mu$m to the focal point. The reason for this is an offset between the calibration plate and the wall and that the position at which the triplets converge to a point has been chosen within the glass in order to have triplets with similar orientation in the wall-bounded measurement volume. Variation of the offset with the image position indicates a slight tilt between the calibration plate and the focal plane, which is compensated latter on by fitting the wall position

y_0 using particle images that stick to the wall.

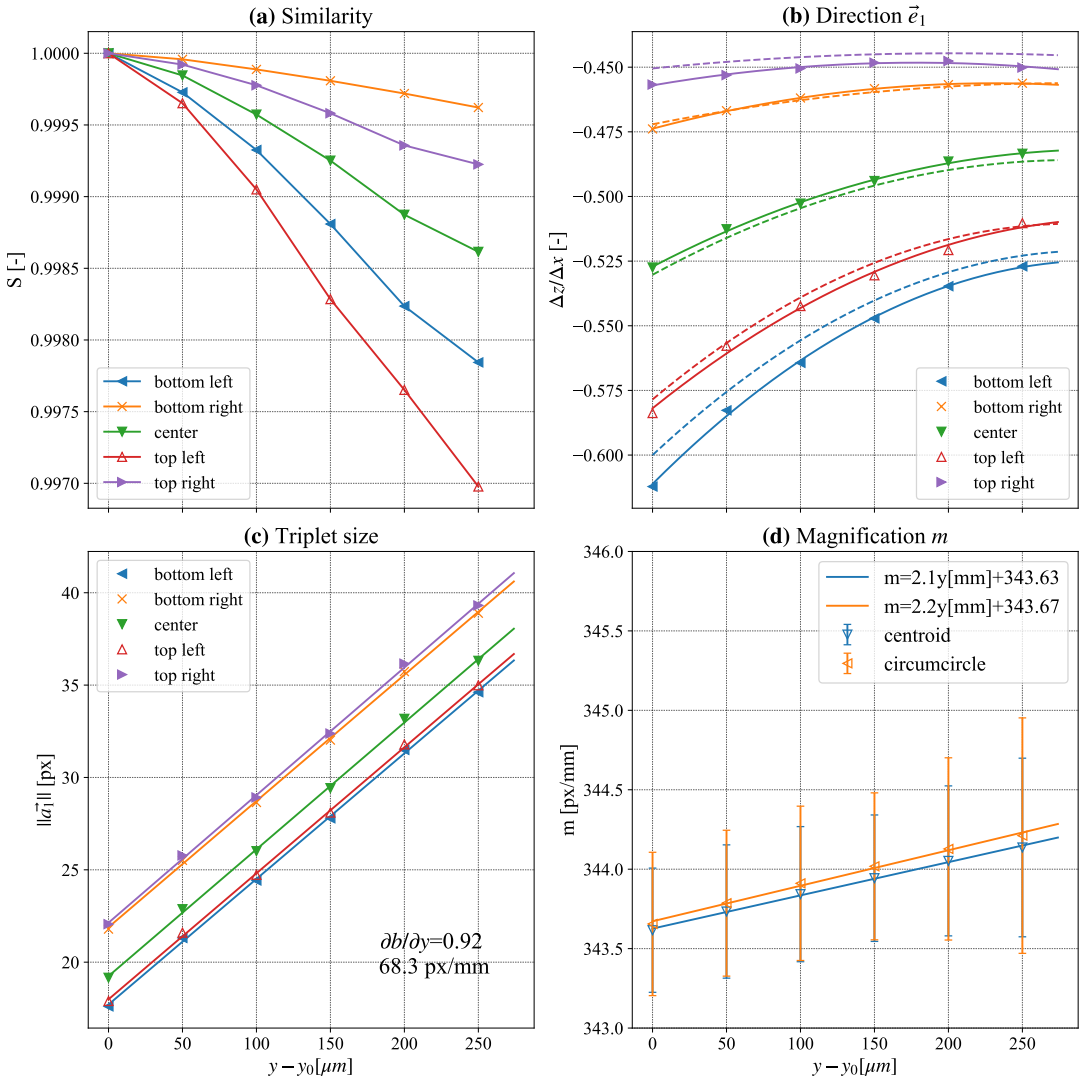

Figure 6. Geometric calibration parameters for various image regions: (a) Similarity with respect to the nearest wall-position of the calibration plate (b) Direction of the triangle side $\vec{e}_1$ including polynomial fit of 2$^{\text{nd}}$ degree (c) calibration curve for $\vec{e}_1$ (d) magnification ; y_0 corresponds to the wall position.

Fig. 6(d) indicates variations of the magnification within the measurement volume evaluated through the mean spacing of triplet centers at node of the calibration plate. The triplet center (i.e. particle's position) was either evaluated using the centroid or the circumcenter of the three vertices. Again, positions of the grid spacing evaluated by the triplet's centroid provides less scattering compared to the circumcenter. Pincushion or barrel distortion effects could not be detected with the optical configuration used, as indicated by the small RMS from the mean magnification per calibration plane of maximum $\pm 0.2\%$.

By inspecting Fig. 6(d) an increasing magnification with the wall-distance y can be observed which

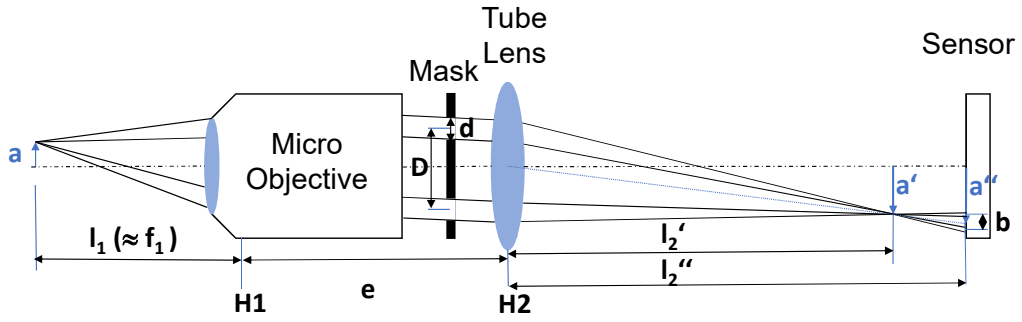

Figure 7. Optical configuration for MA-µPTV with infinity-corrected microscope objective and tube lens.

is contradictory to imaging with a single convex lens where the magnification always decreases with increasing object distance. This deviation is related to the two-stage imaging and is explained in more detail in the following section.

4. Optical characteristics of the MA-µPTV system

The calibration curve in Fig. 6(d) shows that, in contrast to convex singlets, the magnification increases with increasing object distance. This can be explored in more detail by considering the two-stage defocusing optical configuration used here, as shown in Fig. 7, where the image position of a particle is a''. The total magnification between object an sensor plane is $m = m_1\, l_2''/l_2'$, with $m_1 = a'/a$. If the particle is at the focal plane, m_1 becomes $m_f = f_2/f_1$ where f_1 and f_2 are the focal length of microscope objective and tube lens. For small changes in the object distance Δl_1, it can be shown, that the image distance $\Delta l_2'$ varies greatly according to $\Delta l_2' = -m_1^2\, \Delta l_1$. In other words: If the distance of particle to the focal plane increases, the image distance l_1'' decreases by about 20 times this distance in the present configuration. On the other hand, m_1 decreases only slightly with increasing wall distance, which leads to an increase of m in a specific range of e as can be shown by applying the following relations. The total focal length of a system of two thin lenses is

$$f = \frac{f_1\, f_2}{f_1 + f_2 - e} \tag{3}$$

where f_1 and f_2 are the focal length of microscope objective and tube lens and e is the spacing between the principle planes of both lenses (Schröder & Treiber, 2002). The spacing of the image sided principle planes of the overall system then becomes (Schröder & Treiber, 2002)

$$\overline{H_2 H'} = \frac{f_2\, e}{e - f_1 - f_2} \tag{4}$$

In the present MA-µPTV system, e cannot be measured precisely and is estimated with the range $40\,\text{mm} < e < 60\,\text{mm}$, as the actual principal points of the microscope objective and the tube lens are not specified by the manufacturers. By applying the previous equations for the given range of

e in combination with the thin lens equation, it is evident that the total magnification m becomes slightly larger than the focal magnification m_f if $f_1 < e < f_2$ as shown in Fig. 8.

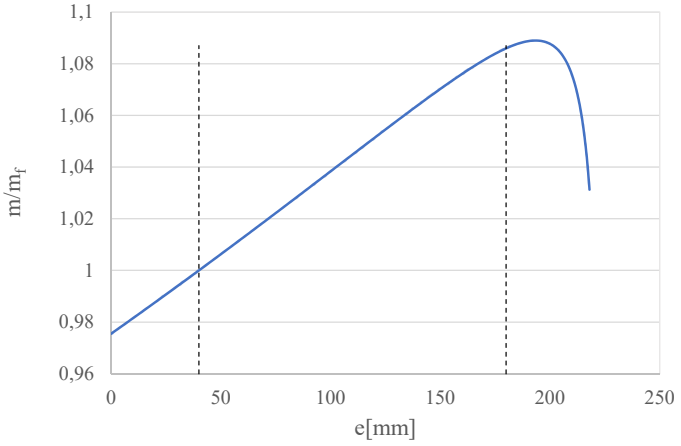

Figure 8. Ratio of the image magnification m at the far edge of the volume and the focal magnification m_f near the wall for different distances between the microscope objective and the tube lens.

5. Triplet image processing

In order to minimize the distortions through window contamination by particle deposition a sliding minimum over 20 frames is subtracted from each image. In a further step particle images are identified by segmentation for which each image is convoluted with a Gaussian template of $\sigma = 1.8$ pixel and 8×8 pixels size. Potential particle images were identified for regions exceeding a given threshold of the normalized cross-correlation coefficient. Image regions segmented in this way were filtered to exclude regions covering an area smaller than a certain threshold, i.e. 6 pixels, since these regions were primarily associated with noise. For the remaining particle image regions the centroids are determined. To map the particle images into triplets, a search is performed on

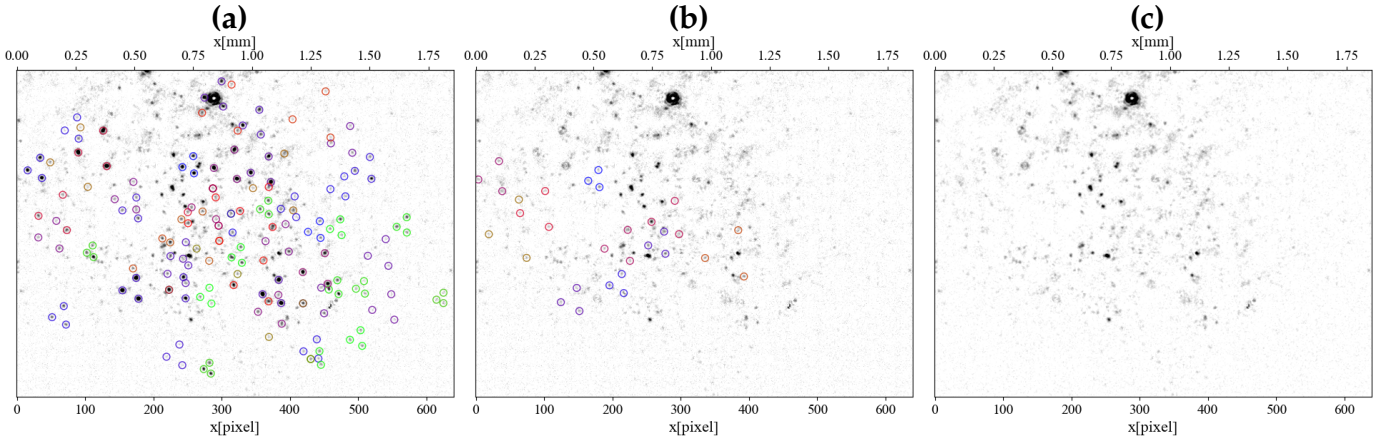

Figure 9. (a) Processed MA-μPTV sample image from Fig. 4(a) with fitted triplets indicated by circles, wall distance is color-coded (b) second iteration on the residual image (c) residual image with fitted intensities subtracted.

the centers to find particle image pairs that belong to the same triplet. Matching is based on the similarity S when comparing $\vec{a}_1$ with the reference vector $\vec{e}_1(x, y, z)$ for which the latter is provided through look-up-table based on calibration data. For particle image pairs above a certain threshold, the neighboring particle images $\vec{a}_2$, $\vec{a}_3$ that maximize the similarity of the triplet are searched for. Once a triplet is identified, the three particle image centers are refined by means of least squares fitting of a 2d Gaussian of predetermined width and the z position is obtained using the calibration curve Fig. 6(c).

To increase the yield for partially overlapping triplet images, the procedure is repeated once on the residual image which is obtained by subtracting the fitted Gaussian distributions.

To estimate the mean width of noisy particle images, a set of images was pre-processed in the manner described above with details provided in Klinner & Willert (2022). The particle images are accumulated separately for each corner (A, B, C) in $8 \times 8 \times 10$ adjacent spatial bins of $233 \times 233 \times 291$ µm^3 size along x, y, z. To do this, the particle images were shifted to a uniform position within windows of 12×12 pixels using third order spline interpolation.

Since a depth position can be determined for each side of the triangle, the maximum absolute deviation between the three positions serves as a disparity measure ϵ.

Fig. 9 shows a sample image processed as described above with (b) and (c) showing the residual images after the first and second iteration. The centers of the particle images resulting from the triplet matching are indicated by circles with the wall distance color-coded. Some skewed triplets can clearly be observed for the given maximum similarity of 0.998. In the residual image Fig. 9(c) the remaining triples are barely distinguishable from the speckled background intensities.

5.1. Determining the wall position

To find the exact wall position y_0 for the determination of $\vec{\tau}_w$, the 3d position of particles sticking to the wall was evaluated, as can be seen, for example, in the stationary triplet particle images in Fig. 4(c). The wall shift was determined from the particle positions on the wall (x, y_0, z) using a linear fit $y_0 = mx + nz + o$. The result is shown in Fig. 11. The mean absolute residuals of the plane fit were $3\,\mu\mathrm{m}$ to $4\,\mu\mathrm{m}$ with a maximum absolute residual of $11\,\mu\mathrm{m}$. It can be observed that with increasing speed in the wind tunnel from $u_{\text{bulk}} = 10\,\mathrm{m/s}$, the wall position is closer to the reference position, presumably due to a decrease in static pressure in the test section. For the series $u_{\text{bulk}} < 20\,\mathrm{m/s}$, average images of each recording were used to determine the wall position. At $u_{\text{bulk}} = 20\,\mathrm{m/s}$, vibrations of the wall in the order of $\pm 2\mu\mathrm{m}$ could be observed (cf. Fig. 11a) and were included in the calculation of the wall shear stress. For this purpose, triplet image processing was carried out on the basis of the sliding minimums over 20 particle images each. Deviations from the mean wall shift were additionally low-pass filtered with a cut-off by 200 Hz (cf. Fig. 11b). The corresponding pre-multiplied power spectral density (PSD) of the wall vibrations shows distinct

peaks of structural vibration near 90 Hz (see Fig. 11b).

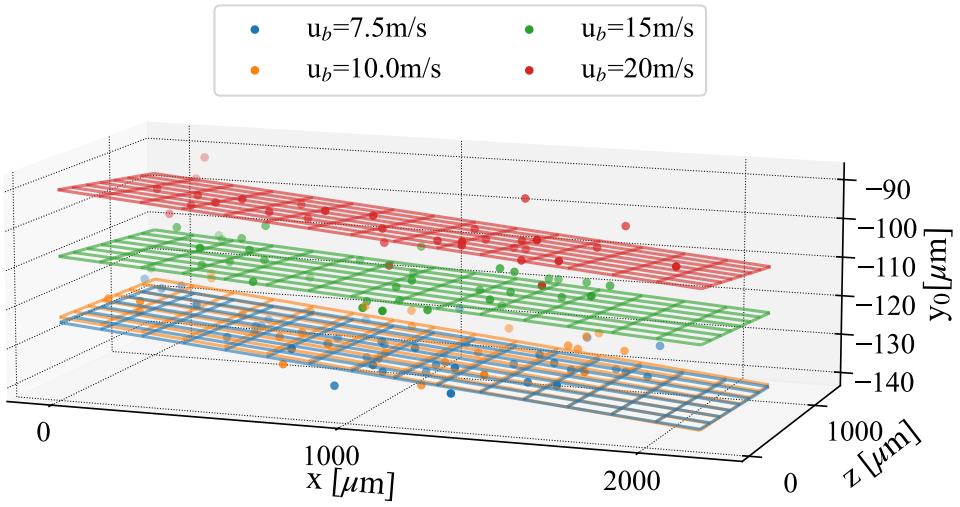

Figure 10. Plane fit of the wall position obtained from particles sticking to the wall.

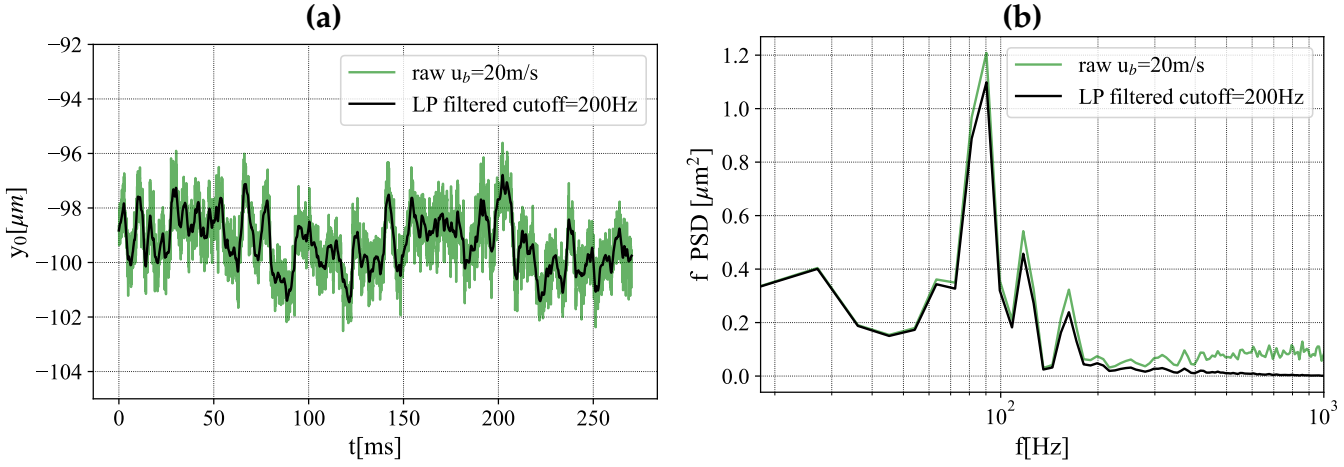

Figure 11. (a) Wall vibration near image center, (b) pre-multiplied power spectrum of wall vibrations by evaluation of sliding minimum images at $u_{\text{bulk}} = 20\,\text{m/s}$.

5.2. Track reconstruction

Lagrangian particle tracks were initialized with up to four image frames using classical techniques as described by Malik et al. (1993) and Ouellette et al. (2006). Starting from the first image, the nearest neighbors in the following image are searched in a domain constrained by a given range of the wall distance variation (10% of Δz), which is considered an appropriate criterion for a wall-bounded flow.

Initialization of the predictors towards the second frame on the basis of neighboring tracks in the first frame (cf. Malik et al., 1993) was discarded here because, due to high shear rates, only neigh-

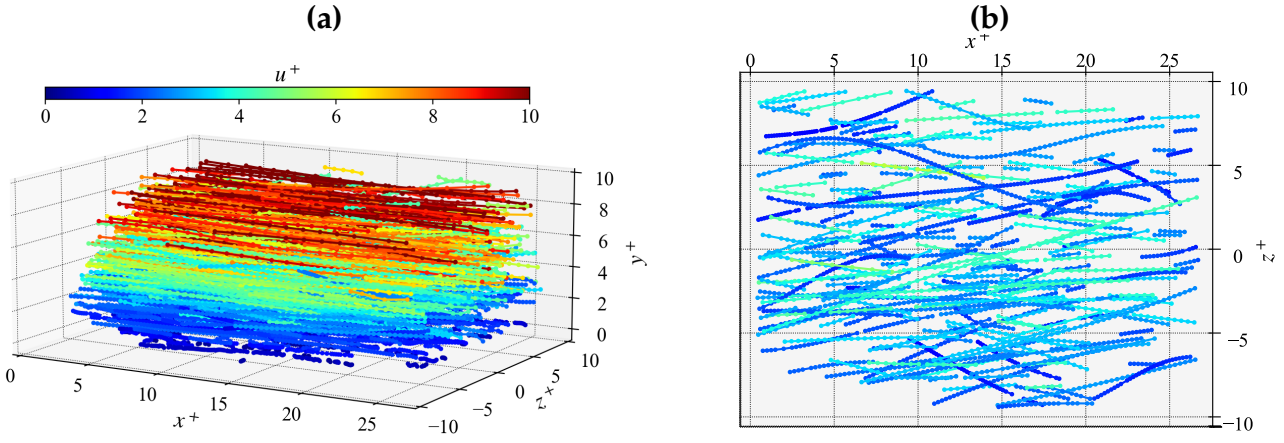

Figure 12. (a) An accumulation of 0.2% (2000) of the total number of tracks at $u_{\text{bulk}} = 5.2\,\text{m/s}$, $\text{Re}_\tau = 563$, $l^* = 69\mu\text{m}$, extracted from 1680 images captured at 28 kfps (b) spanwise meandering tracks in $2 < y^+ < 3$ (x-z projection).

bors with approximately equal wall distance and only within a search radius of the Kolmogorov length scale can be considered, which rarely occur at the present low particle image density. On the other hand, the same particle may occasionally disappear and then reappear in the following frame due to varying intensity levels or speckle noise. Therefore, the third frame is also included in the nearest neighbor search if no candidate is found in the second frame. Using the displacements between possible particle matches as predictors, candidates are targeted in the third frame within a constant maximum search radius. In the present case, the maximum search radius was set to a constant value $r_{\text{max}} = u'_{\text{max}}\,\Delta t/M$, where u'_{max} was estimated according to the near-wall maximum of the streamwise velocity fluctuation u' in a ZPG TBL ($u'_{max} \approx \sqrt{8}u_\tau$). If no suitable candidate is found, the fourth frame is also included using twice the previous displacements. From candidates that are linked in three frames, the track with smallest change in velocity is selected (e.g. minimum acceleration criterion). To continue tracks from length three, the predicted displacement toward following frames base on the velocity difference to the predecessor plus the displacement extrapolated from the acceleration in the previous two frames. For longer tracks, the predictor bases on a cubic b-spline fitted through the last four track members. After forward tracking is performed over a set of frames, shortest tracks that consist of less then 4-5 members are removed. With the spurious tracks removed, the entire tracking procedure is repeated for the remaining unlinked particles in backward time association, followed by removal of short tracks. A compilation of $0.2\,\%$ of the tracks recorded at $u_{\text{bulk}} = 5.2\,\text{m/s}$ is shown in Fig. 12a and demonstrates multiple tracks within the viscous sublayer and a clear spatial variation in velocity within the sublayer with a sharp drop in flow velocity as the wall is approached. In addition, Fig. 12(b) demonstrates the occurrence of linear high speed and meandering low speed tracks also observed in earlier experiments in TBL flows (Fage et al., 1932; Kumar et al., 2021).

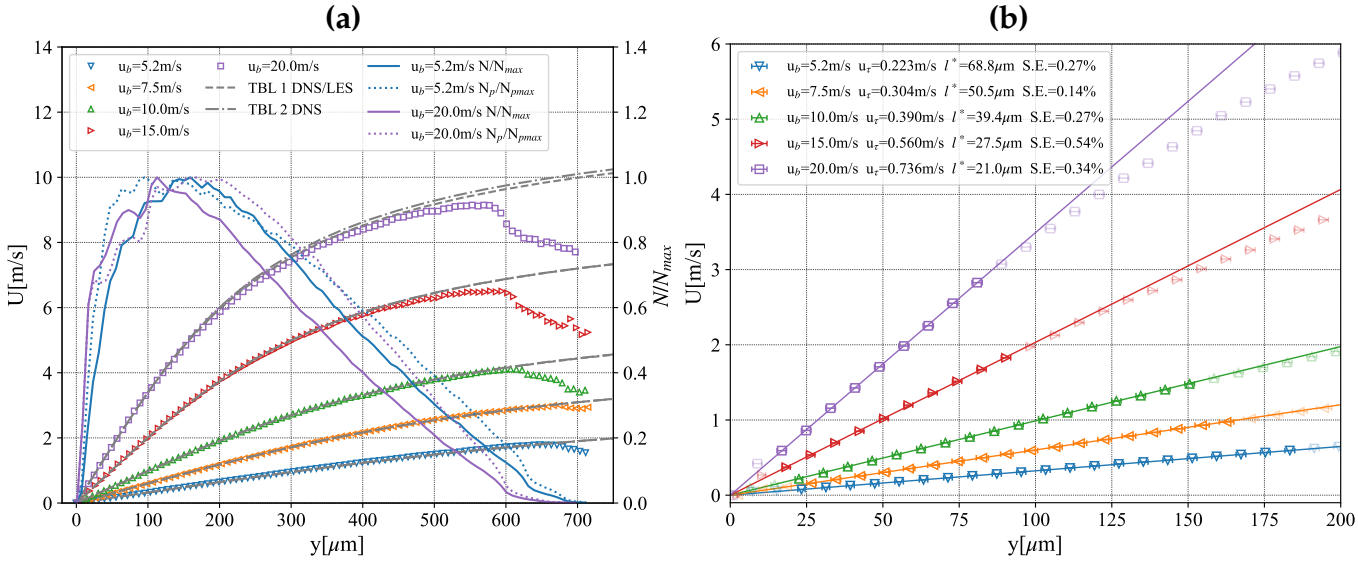

Figure 13. Mean streamwise velocities from bin averaging of MA-μPTV data (bin width = 8μm): (a) Supplemented by bin counts at the minimum and maximum bulk velocity and profiles form numerical simulations TBL1 (Schlatter & Örlü, 2010a) and TBL2 (Sillero et al., 2013) (b) mean near-wall velocity and linear fit to obtain the wall gradient in $0 < y^+ < 4$ (fading symbols are excluded from the fit, error bars indicate the mean absolute disparity).

6. Results and Discussion

To allow comparison with flow statistics obtained with high-speed profile PIV and numerical data, a bin-averaging scheme with bin-heights of $8\,\mu\mathrm{m}$ ($\leq 0.5\,l^*_{min}$) in wall normal direction was used. Therefore, the velocity at each particle position is obtained from the first derivative of cubic b-splines fitted over the vertices of each track using *splprep*() of the *SciPy* package (Virtanen et al., 2020). Based on the absolute disparity ϵ in each vertex, spline smoothing is applied by setting the parameter $s = n\,\epsilon^2$, with n being the number of vertices, which enables better agreement with variance profiles from DNS as will be shown later in this section. The assignment into equally spaced bins is performed using bilinear weighting.

In Fig. 13(a), the profiles of the mean axial velocity determined in this way are compared with profiles from DNS/LES and supplemented by the bin counts. In addition, the number of particles N_p (e.g. number of tracks) detected over the wall distance is represented by the dotted lines. While a steep increase in particle counts up to the maximum can be seen on the side near the wall, they decrease continuously from a wall distance of $100\,\mu\mathrm{m}..150\,\mu\mathrm{m}$ up to a distance of $650\,\mu\mathrm{m}..700\,\mu\mathrm{m}$, with the bin counts decreasing almost linearly. Near the wall, the differences in the number of particles between the lowest and highest bulk velocities could be related to the inertia of the particles, with the number of particles being lower at high velocities. Toward the far volume edge, the decrease in particle counts is most likely due to the restricted depth of focus of the method, in which the image intensity has decreased at a greater distance from the focus, making them less detectable. Similarly the increased degree of turbulence in the buffer layer leads to a decreased number of

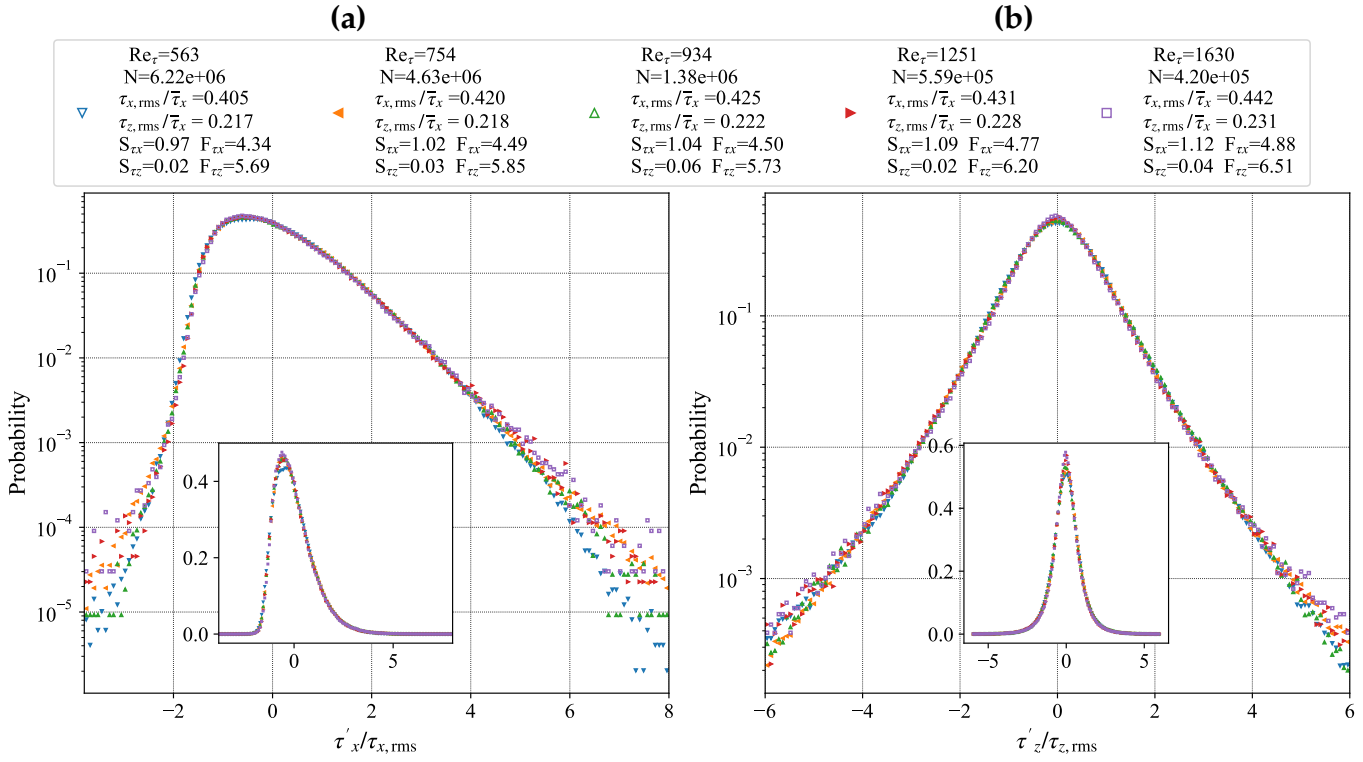

Figure 14. (a) streamwise and (b) spanwise distributions of the wall shear rate as determined with MA-µPTV.

linked particles. In addition, an earlier decrease of bin counts at the higher bulk velocity is due to the camera limitations as the frame rate could not be increased in the same proportion. Therefore, at lower bulk velocities ($u_{\mathrm{bulk}} < 10\,\mathrm{m/s}$), the mean velocities agree well up to wall distances of $650\,\mu\mathrm{m}$ ($9.4\,l^*..13\,l^*$) despite very reduced bin counts. For the reasons mentioned, an underestimation of the mean velocity occurs with increasing velocity and wall distance from about $y > 500\mu\mathrm{m}$ ($y^+ > 13$) for $u_{\mathrm{bulk}} = 10\,\mathrm{m/s}$, from $y > 350\,\mu\mathrm{m}$ ($y^+ > 13$) for $u_{\mathrm{bulk}} = 15\,\mathrm{m/s}$ and from $y > 170\,\mu\mathrm{m}$ ($y^+ > 8$) for $u_{\mathrm{bulk}} = 20\,\mathrm{m/s}$ with respect profiles from DNS. However, it may still be possible to increase the track length far from the wall by reducing the magnification m while maintaining the same frame rate, but at the expense of the accuracy of near-wall velocities and a decreased sensitivity.

Fig. 13(b) provides the mean near wall velocities as obtained from bin averaging of particle tracks. The mean WSS is evaluated by a linear least squares fit. To ensure values inside the linear range only wall distances up to $y^+ < 4$ were considered (faded symbols indicate excluded data points). Friction velocities and viscous units obtained by this method are provided in the plot legend. Also shown in the plot legend is the gradient fit standard error (s.e.) on the linear least square fit according to Hutchins & Choi (2002), which is between $0.14\,\%$ to $0.54\,\%$. The vertical error bars represent the mean absolute disparity of the depth reconstruction which is on the order of $1 - 2.5\,\mu\mathrm{m}$.

Fig. 14 provide the stream- and spanwise probability density distributions of the WSS components τ_x' and τ_z' evaluated in the viscous sublayer ($0.6 < y^+ \leq 4$). Per condition the total sample counts range from $0.42 - 6.2 \times 10^6$. To collapse the data for different Reynolds numbers, the unsteady wall shear rates are normalized by subtracting the mean and by dividing by the RMS. Still some Reynolds number dependency is apparent at the positive tails of τ_x' which indicates a higher probability of extreme positive events and confirms similar observations in numerical studies (Hu et al., 2006; Diaz-Daniel et al., 2017). The spanwise probability density distribution qualitatively indicates deviation from a Gaussian distribution with higher probability in the distribution tails also indicated by values above 3.0 for the flatness, meaning that extreme shear stress events have higher probability compared to a Gaussian.

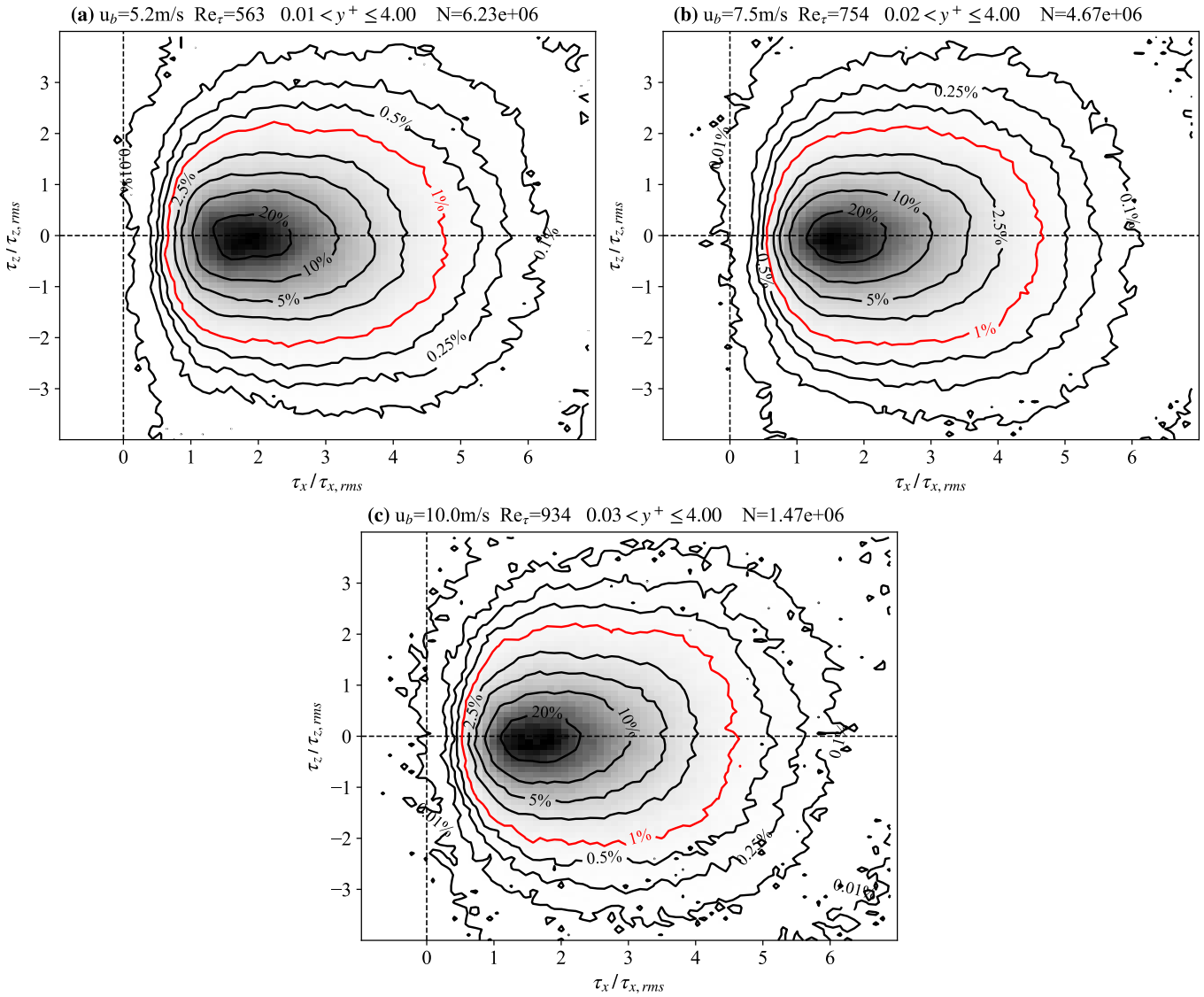

Figure 15. Joint probability distributions of the stream- and spanwise fluctuations of the WSS (a) $u_{\text{bulk}} = 5.2\,\text{m/s}$ (b) $u_{\text{bulk}} = 7.5\,\text{m/s}$ (c) $u_{\text{bulk}} = 10\,\text{m/s}$

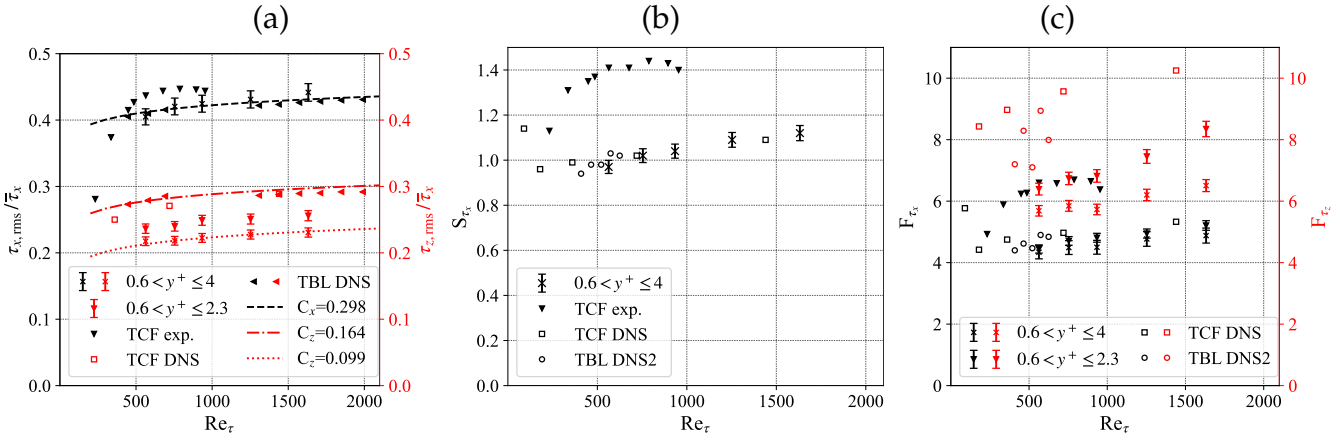

Figure 16. Higher order statistics of streamwise (black symbols) and spanwise (red symbols) components of the WSS; MA-µPTV data as determined from particle tracks in the viscous sub-layer at $0.6 < y^+ \leq 2.3$ (▼,▼) and $0.6 < y^+ \leq 4$ (×, ×) including an uncertainty of 3%; TCF DNS: Hu et al. (2006) TBL DNS: Sillero et al. (2013) TBL DNS2: Diaz-Daniel et al. (2017) TCF exp.: measurements with cavity hot-wire (Gubian et al., 2019) (a) Root mean squared fluctuations of WSS; lines correspond to Eq. 5 with different offsets C_i (b) skewness S_{τ_x} (c) flatness F_{τ_i} (normal distribution: $F_{\tau_i} = 3$).

Fig. 15 shows the corresponding joint probability of stream- and spanwise fluctuations of the WSS vector for different bulk velocities. In order to suppress the distortion of the RMS by particles interacting with the wall, the interval for joint propability estimations starts at a wall distance of $\approx$ 1µm. Reverse flow events appear to occur with an extremely low probability on the order of 10^{-4}, but require further investigation and confirmation by inspection of corresponding tracks.

In current literature correlations are provided for the Reynolds-number dependency of the root mean square (rms) of WSS components of the form

$$\tau_{i,\mathrm{rms}}/\tau_x = C_i + 0.018\, ln(\mathrm{Re}_\tau) \tag{5}$$

for which $C_x = 0.298$ is proposed by Örlü & Schlatter (2011) for the streamwise fluctuations $\tau_{x,\mathrm{rms}}/\tau_x$ based on previous computational and experimental results. Fig. 16(a) indicates agreement to that correlation which involves a maximum residual of 2.4%.

For the spanwise fluctuation $\tau_{z,\mathrm{rms}}$ Diaz-Daniel et al. (2017) proposed the same logarithmic dependence and a value of $C_z = 0.164$ based on DNS in the range $409 \leq \mathrm{Re}_\tau \leq 625$ (cf. dashed dotted line in Fig. 16(a)). Although the same logarithmic dependence is confirmed, the current experiment suggests a significantly lower offset of $C_z = 0.099$ with a maximum residual of 2%, as indicated by the dotted line in Fig. 16(a). This result is qualitatively inline with experimental results obtained at $\mathrm{Re}_\tau = 400$ by Kumar et al. (2021) who also observed a decrease of $\tau_{z,\mathrm{rms}}$ in comparison to values reported from DNS. It is assumed that the underestimation can be explained by the rapid decrease of the spanwise fluctuations w_{rms}/U with increasing wall distance, as predicted from DNS data and as described in more detail in Willert & Klinner (2024). Fig. 16(a) shows a MA-µPTV data series in which $\tau_{z,\mathrm{rms}}$ was determined in the interval $0.6 < y^+ \leq 2.3$ which confirms the trend towards

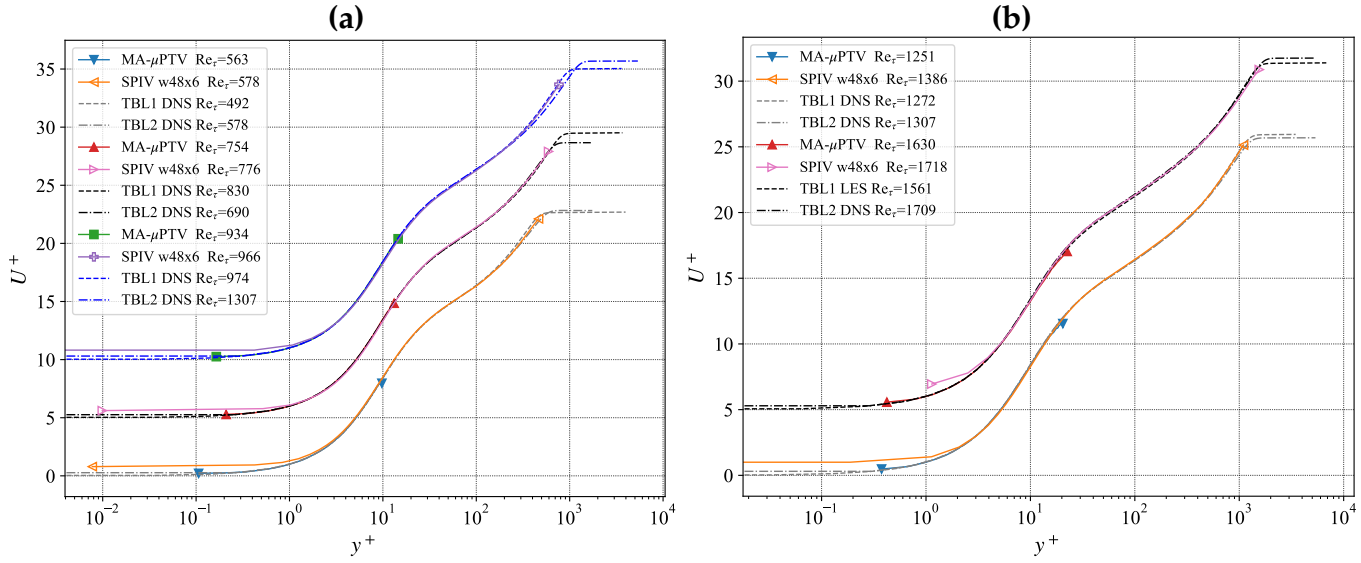

Figure 17. Mean streamwise velocities at inner scaling supplemented by profiles from SPIV and numerical simulations of a ZPG TBL1 (Schlatter & Örlü, 2010a) and TBL2 (Sillero et al., 2013); velocities are offset by $5u^+$ (a) $u_{\text{bulk}} = 5.2,\ 7.5,\ 10.0\,\text{m/s}$ (b) $u_{\text{bulk}} = 15,\ 20\,\text{m/s}$.

higher spanwise fluctuations in comparison to statistics from $0.6 < y^+ \leq 4$.

The skewness of the streamwise WSS distributions (cf. Fig. 16b) is near unity and agrees well to values reported from DNS of a turbulent channel by Hu et al. (2006) for the given range of Reynolds-numbers and is within $3\,\%$ deviation. Although not plotted here, values for skewness of the spanwise component of the WSS are near zero with a maximum deviation of 5% as indicated also by values in the legend in Fig. 14.

Fig. 16(c) provides the flatness (kurtosis) of the WSS where the present $F_{\tau x}$ values are slightly lower in comparison to values from DNS reported by Hu et al. (2006) for a turbulent channel flow (TCF) as well as by Diaz-Daniel et al. (2017) for a ZPG TBL. Nonetheless, the current experimental values are still within a maximum absolute deviation of $8\,\%$. An underestimation can be observed for the spanwise flatness F_{τ_z} where DNS data reported in the literature indicate a larger probability of extreme events in comparison to the present measurements. This is also reflected in a reduced spanwise fluctuation $\tau_{z,\text{rms}}$ in the measurements when compared to DNS. The wall distance also appears to have a major influence here, as the flatness also increases significantly with decreasing wall distance when inspecting values obtained at $0.6 < y^+ \leq 2.3$ in comparison to values at $0.6 < y^+ \leq 4$.

Mean velocity profiles for all free stream conditions are provided in Fig. 17, normalized by the corresponding viscous unit and friction velocity. HS profile-PIV indicates a clear logarithmic region and the beginning of the wake region as expected for this type of flow.

Up to the beginning of the logarithmic region the mean streamwise velocity agrees well with DNS

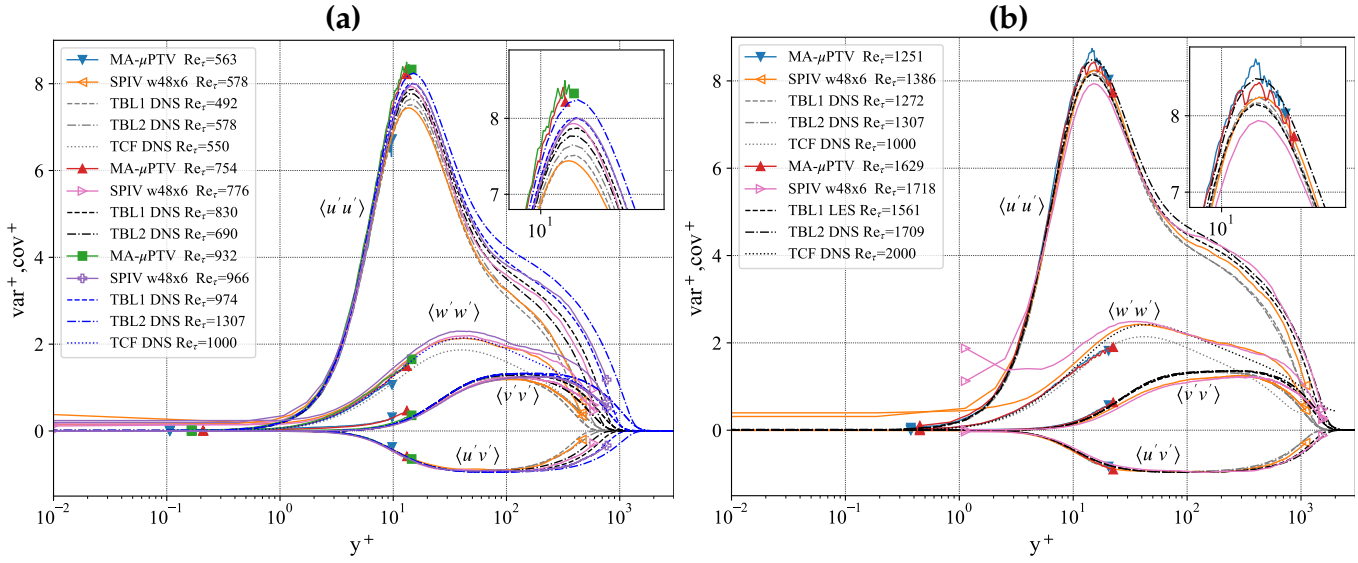

Figure 18. Fluctuating velocities at inner scaling supplemented by profiles from SPIV and numerical simulations of a ZPG TBL1 (Schlatter & Örlü, 2010a) and TBL2 (Sillero et al., 2013) and of a TCF by Lee & Moser (2015) (a) $u_{\text{bulk}} = 5.2,\ 7.5,\ 10.0\,\text{m/s}$ (b) $u_{\text{bulk}} = 15,\ 20\,\text{m/s}$.

and LES data of a ZPG TBL from two sources (Schlatter & Örlü, 2010b; Sillero et al., 2013), which is an important 'proof of concept' for an accurate determination of both: near-wall velocities and inner scaling with MA-μPTV. In the outer regions the mean velocity is underestimated and indicates the limitations of the present configuration ($m = 4.5$, $d = 2$, $D = 8.2$). This was already discussed at the beginning of this section that depending on friction velocity 0.223 m/s to 0.736 m/s underestimation occurs from wall distances of $8\,l^*$ to $13\,l^*$.

It can be seen that HS profile SPIV and MA-μPTV are complementary techniques that cover different regions of the boundary layer profile with overlap in the buffer layer. While high near-wall gradients are a challenge for profile PIV, even with narrow window sizes of 48×6 pixels, the region of the viscous sublayer ($y^+ < 4$) can only be captured reliably using PTV.

Fig. 18 indicates that $\langle u'u' \rangle$ agrees well to profiles from DNS and LES up to $y^+ = 8$. Beyond this wall distance, limitations in the focal depth of MA-μPTV and the lower proportion of fast tracks result in less converged second order statistics and an overestimation of the streamwise variance. With increasing friction velocity the "inner peak" shifts toward the wall, to $y \approx 230\mu$m at $u_{\text{bulk}} = 20$m/s, and the over-estimation seems to be partially compensated with the increase in bin counts ($\approx 0.7\%$ of the maximum sample counts). The peak height, although not converged, is reproduced within the range provided by numerical simulations in Fig. 18(b). Deviations in the peak height for HS profile SPIV were not yet sufficiently clarified at the time of writing this contribution, but most likely are due to the spatial filtering of small structures by the finite sized interrogation window or due to overestimation of u_τ when using the Clauser chart method (Clauser, 1956).

Both MA-μPTV and HS profile PIV reproduce the profiles of the wall-normal variance $\langle v'v' \rangle$ pre-

dicted by DNS/LES up to $y^+ < 20$. Here MA-µPTV consistently provides slightly higher at the lower bulk velocites $u_{\mathrm{bulk}} < 10\mathrm{m/s}$ (cf. Fig. 18(a)) while more accurately reproducing $\langle v'v' \rangle$ at higher velocities when a threshold in track length of $n > 5$ was applied. In fact, different thresholds of the track length was found to affect the results: For the lower bulk velocities, track lengths with a minimum length of 5 ($n > 4$) were allowed, which lead to a lower standard error of $\overline{\tau_w}$ and a later underestimation of the axial component with increasing wall distances, at the cost of a larger inaccuracy of $\langle v'v' \rangle$ due to shorter tracks in comparison to a track length threshold of 6 ($n > 5$). In future measurements, this effect could be compensated by increasing the frame rate and/or image size when using faster HS cameras.

Since the previously cited numerical databases of ZPG TBL flows do not provide spanwise variance $\langle w'w' \rangle$, DNS simulations of a TCF by Lee & Moser (2015) were chosen here as a reference for comparison. While profiles obtained with HS SPIV indicate over prediction of the spanwise variances for wall distances $y^+ < 30$, the deviations for MA-µPTV are significantly smaller. While the profiles of the spanwise variance measured with MA-µPTV for $750 \leq \mathrm{Re}_\tau \leq 932$ closely match the DNS of the TCF at $\mathrm{Re}_\tau = 1000$, these are somewhat overestimated for $\mathrm{Re}_\tau = 563$ from $y^+ \geq 2$ and for $\mathrm{Re}_\tau = 1251$ from $y^+ \leq 8$ and only from $y^+ \geq 8$ rather underestimated for $\mathrm{Re}_\tau = 1629$ probably due to the lower sample count. In general, for MA-µPTV the spanwise variance in the viscous sublayer ($y^+ < 4$) is very slightly overestimated compared to the DNS profiles, which means that it can actually be excluded that uncertainties in the near-wall span velocities are the cause of discrepancies between numerical and experimental data in $\tau_{z,\mathrm{rms}}$ in Fig. 16(a). For HS profile SPIV the over-prediction of the spanwise component could be caused by the low opening angle between the cameras of about $25°$ which involves a three times larger uncertainty of the spanwise component in comparison to the streamwise component.

Remarkably, Fig. 19 indicates, that for the lowest Re_τ, profiles of streamwise skewness S_u and flatness F_u of the streamwise velocity u from MA-µPTV coincide very well with values from DNS in the range of measurement $0.2 \leq y^+ \leq 10$, although more data is required to get a smooth curve. For the remainder of the test points, the skewness (cf. Fig. 19(a)) agrees with DNS in the range $2 \leq y^+ \leq 6$. Deviation from DNS above a wall distance $y^+ > 6$ is probably related to decreased bin count. Also, the under-representation of faster tracks in the buffer layer and the overestimation of the variance due to increasing noise seem to result in an overestimation of the skewness with respect to the DNS. On the other hand, for $\mathrm{Re}_\tau \geq 754$ and from $y^+ = 1..2$, the measured flatness F_u agrees very well to values from DNS within the measurement uncertainty related to a sample counts which were too low to achieve convergence (cf. Fig. 19b).

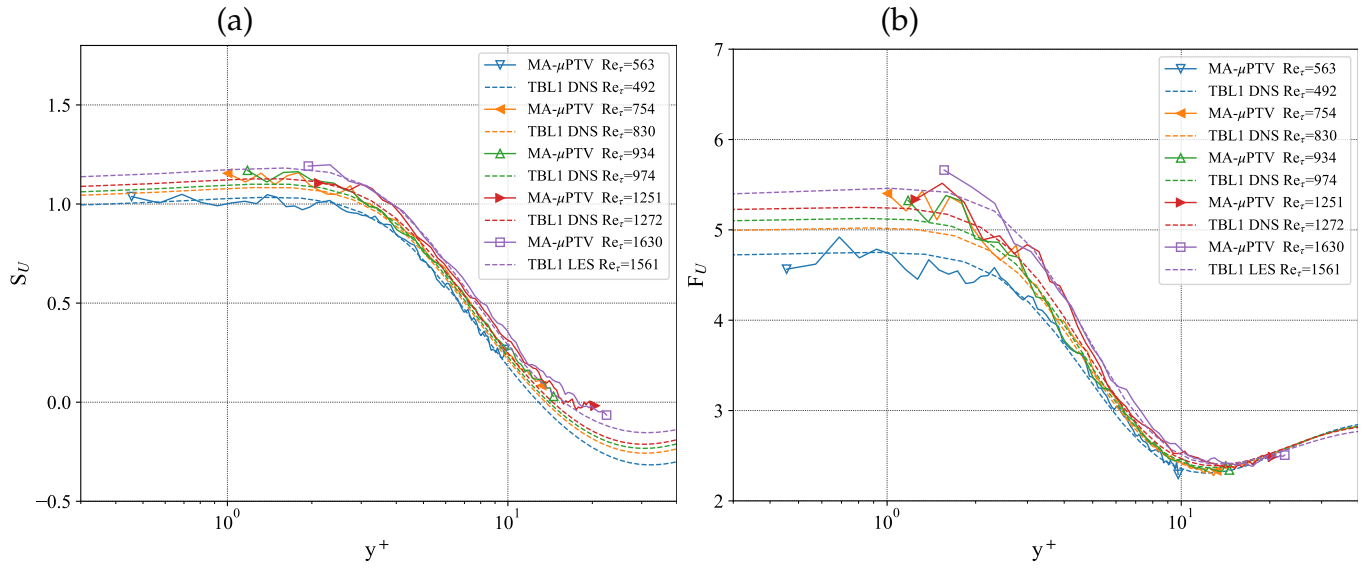

Figure 19. (a) Skewness S_u and (b) flatness F_u of axial velocities supplemented by profiles from numerical simulations of a ZPG TBL by Schlatter & Örlü (2010a).

Conclusion & Outlook

The present results give a strong indication that MA-μPTV is a viable non-contact technique for measurements of the unsteady wall shear stress vector using only a single access port. The equipment requirements are relatively low compared to setups relying on multiple camera configurations with side-scattering illumination.

In the viscous sublayer, the probability density distributions of both, stream- and spanwise WSS, could be reliably captured down to probability densities of 10^{-3}. As far as we know, this has not been achieved in the past, particularly not for the spanwise component. For the streamwise component the measured Reynolds-number dependency of $\tau_{i,\mathrm{rms}}$ agrees to correlations by Örlü & Schlatter (2011) with a maximum residuum of 2.4%. Furthermore, the skewness of the streamwise WSS S_{τ_x} agrees well to values from literature with maximum deviations of 53%. The discrepancy of the spanwise $\tau_{z,\mathrm{rms}}$ between DNS and current measurement needs further investigation. At this point, it is assumed that the cause of the underestimation can be explained by the rapid decrease of the spanwise fluctuations w_{rms}/U with increasing wall distance. Furthermore, at the time of writing, there is no plausible explanation that could be related to specifics of the experimental imaging setup. A similar underestimation has also been observed by Kumar et al. (2021), but limited to a single Reynolds number ($\mathrm{Re}_\tau \approx 400$) that was at the lower end of the current study.

Wall-normal profiles of 3c velocity statistics were obtained at a spatial resolution of $8\,\mu\mathrm{m}$ ($\leq 0.5\,l^*_{min}$) or $0.6\,\mathrm{pixel}$ for which the mean absolute disparity per bin was $1\,\mu\mathrm{m}..2.5\,\mu\mathrm{m}$ or $0.1\,\mathrm{pixel}..0.2\,\mathrm{pixel}$. Up to the buffer layer, profiles of the mean streamwise velocity agree well with DNS and LES of a ZPG TBL, which indicates an accurate determination of both: near-wall velocities and inner scaling.

The depth-of-field beyond which the mean flow velocity begins to be underestimated represents the upper spatial limit of the present configuration ($f_{max} = 37\,\mathrm{kHz}$, $m = 4.5$, $d = 2\mathrm{mm}$, $D = 8.2\mathrm{mm}$). For the present range of friction velocities of $0.223\mathrm{m/s} \leq u_\tau \leq 0.736\mathrm{m/s}$ these upper limits are in the range of $250\,\mu$m to $650\,\mu$m along y.

In conclusion, it can be stated that measurements of the unsteady wall shear stress vector at unprecedented levels of accuracy and resolution are presented herein. It is important to note, that the applicability of the technique does not depend on the shear Reynolds number of the flow itself, which also depends on BL thickness, but rather on the size of the viscous unit. Using faster cameras this could be further increased to much higher u_τ as resolving viscous scales down to O(10 µm) is feasible with the current lens magnification. As an alternative, high magnification 3D-STB Schanz et al. (2016) holds similar potential but requires 3-4 high-speed cameras. By using modern high-speed cameras with frame rates exceeding 40 kHz along with a 3-4 times longer field of view (FOV) in streamwise direction would extend the velocity range and thus the depth of the measurement volume by increasing the yield in longer tracks in the buffer layer. To reduce the problem of low particle image density and thus achieve a higher number of samples per data set, a larger field of view should be captured, e.g. by using microscope optics with lower magnification in combination with cameras with smaller pixels, which in turn requires a proportionally higher laser power to obtain the same signal-to-noise ratio of the triplet particle images.

References

Barnkob, R., & Rossi, M. (2020). General defocusing particle tracking: fundamentals and uncertainty assessment. *Exp Fluids*, *61*, 110. Retrieved from `https://doi.org/10.1007/s00348-020-2937-5` doi: 10.1007/s00348-020-2937-5

Cardesa, J. I., Monty, J. P., Soria, J., & Chong, M. S. (2019). The structure and dynamics of backflow in turbulent channels. *Journal of Fluid Mechanics*, *880*, R3. doi: 10.1017/jfm.2019.774

Chen, S., Angarita-Jaimes, N., Angarita-Jaimes, D., Pelc, B., Greenaway, A. H., Towers, C. E., ... Towers, D. P. (2009). Wavefront sensing for three-component three-dimensional flow velocimetry in microfluidics. *Experiments in Fluids*, *47*, 849. Retrieved from `https://doi.org/10.1007/s00348-009-0737-z` doi: 10.1007/s00348-009-0737-z

Cierpka, C., Scharnowski, S., & Kähler, C. J. (2013). Parallax correction for precise near-wall flow investigations using particle imaging. *Applied Optics*, *52*(12), 2923–2931. Retrieved from `https://opg.optica.org/ao/abstract.cfm?uri=ao-52-12-2923` (Publisher: Optica Publishing Group) doi: 10.1364/AO.52.002923

Cierpka, C., Segura, R., Hain, R., & Kähler, C. J. (2010). A simple single camera 3c3d velocity measurement technique without errors due to depth of correlation and spatial averaging for microfluidics. *Measurement Science and Technology*, *21*(4), 045401. Retrieved from https://doi.org/10.1088/0957-0233/21/4/045401 doi: 10.1088/0957-0233/21/4/045401

Clauser, F. H. (1956). The turbulent boundary layer. In H. L. Dryden & T. v. Kármán (Eds.), (Vol. 4, pp. 1–51). Elsevier. Retrieved from https://doi.org/10.1016/S0065-2156(08)70370-3 doi: https://doi.org/10.1016/S0065-2156(08)70370-3

Diaz-Daniel, C., Laizet, S., & Vassilicos, J. C. (2017). Wall shear stress fluctuations: Mixed scaling and their effects on velocity fluctuations in a turbulent boundary layer. *Physics of Fluids*, *29*(5), 055102. Retrieved from https://aip.scitation.org/doi/10.1063/1.4984002 doi: 10.1063/1.4984002

Fage, A., Townend, H. C. H., & Taylor, G. I. (1932). An examination of turbulent flow with an ultramicroscope. *Proceedings of the Royal Society of London. Series A, Containing Papers of a Mathematical and Physical Character*, *135*(828), 656–677. (Publisher: Royal Society) doi: 10.1098/rspa.1932.0059

Fuchs, T., Bross, M., & Käähler, C. J. (2023). Wall-shear-stress measurements using volumetric µPTV. *Experiments in Fluids*, *64*(6), 115. doi: 10.1007/s00348-023-03656-1

Fuchs, T., & Kähler, C. J. (2019). Single axis volumetric μPTV for wall shear stress estimation. In *Proceedings of the 13th International Symposium on Particle Image Velocimetry.* Retrieved from https://athene-forschung.unibw.de/129386

Gubian, P.-A., Stoker, J., Medvescek, J., Mydlarski, L., & Baliga, B. R. (2019). Evolution of wall shear stress with reynolds number in fully developed turbulent channel flow experiments. *Phys. Rev. Fluids*, *4*(7), 074606. Retrieved 2024-05-29, from 10.1103/PhysRevFluids.4.074606 (Publisher: American Physical Society) doi: 10.1103/PhysRevFluids.4.074606

Hu, Z. W., Morfey, C. L., & Sandham, N. D. (2006). Wall pressure and shear stress spectra from direct simulations of channel flow. *AIAA Journal*, *44*(7), 1541–1549. Retrieved from https://arc.aiaa.org/doi/10.2514/1.17638 (Publisher: American Institute of Aeronautics and Astronautics) doi: 10.2514/1.17638

Hutchins, N., & Choi, K.-S. (2002). Accurate measurements of local skin friction coefficient using hot-wire anemometry. *Progress in Aerospace Sciences*, *38*(4), 421–446. Retrieved from https://doi.org/10.1016/S0376-0421(02)00027-1 doi: 10.1016/S0376-0421(02)00027-1

Klinner, J., & Willert, C. (2022). Feasibility of multi-aperture micro-ptv for wall shear stress measurements. In *20th international symposium on application of laser and imaging techniques to fluid mechanics.* Retrieved from https://elib.dlr.de/187946/

Kumar, S. S., Huang, X., Yang, X., & Hong, J. (2021). Three dimensional flow motions in the viscous sublayer. *Theoretical and Applied Mechanics Letters*, *11*(2), 100239. Retrieved from https://www.sciencedirect.com/science/article/pii/S2095034921000465 doi: https://doi.org/10.1016/j.taml.2021.100239

Lee, M., & Moser, R. D. (2015). Direct numerical simulation of turbulent channel flow up to $\mathrm{Re}_\tau \approx 5200$. *Journal of Fluid Mechanics*, *774*, 395–415. Retrieved from https://doi.org/10.1017/jfm.2015.268 doi: 10.1017/jfm.2015.268

Lenaers, P., Li, Q., Brethouwer, G., Schlatter, P., & Örlü, R. (2011). Negative streamwise velocities and other rare events near the wall in turbulent flows. *Journal of Physics: Conference Series*, *318*(2), 022013. doi: 10.1088/1742-6596/318/2/022013

Lu, J., Pereira, F., Fraser, S. E., & Gharib, M. (2008). Three-dimensional real-time imaging of cardiac cell motions in living embryos. *Journal of Biomedical Optics*, *13*(1), 014006. Retrieved from https://doi.org/10.1117/1.2830824 doi: 10.1117/1.2830824

Malik, N. A., Dracos, T., & Papantoniou, D. A. (1993). Particle tracking velocimetry in three-dimensional flows. *Experiments in Fluids*, *15*(4), 279–294. Retrieved from https://doi.org/10.1007/BF00223406 doi: 10.1007/BF00223406

Örlü, R., & Schlatter, P. (2011). On the fluctuating wall-shear stress in zero pressure-gradient turbulent boundary layer flows. *Physics of Fluids*, *23*(2), 021704. Retrieved from https://aip.scitation.org/doi/10.1063/1.3555191 doi: 10.1063/1.3555191

Ouellette, N. T., Xu, H., & Bodenschatz, E. (2006). A quantitative study of three-dimensional Lagrangian particle tracking algorithms. *Experiments in Fluids*, *40*(2), 301–313. Retrieved from https://doi.org/10.1007/s00348-005-0068-7 doi: 10.1007/s00348-005-0068-7

Pereira, F., & Gharib, M. (2002). Defocusing digital particle image velocimetry and the three-dimensional characterization of two-phase flows. *Measurement Science and Technology*, *13*(5), 683. Retrieved from http://stacks.iop.org/0957-0233/13/i=5/a=305 doi: 10.1088/0957-0233/13/5/305

Pereira, F., Gharib, M., Dabiri, D., & Modarress, D. (2000). Defocusing digital particle image velocimetry: a 3-component 3-dimensional DPIV measurement technique. application to bubbly flows. *Experiments in Fluids*, *29*(1), S078–S084. Retrieved from https://doi.org/10.1007/s003480070010 doi: 10.1007/s003480070010

Pereira, F., Lu, J., Castaño Graff, E., & M, G. (2007). Microscale 3d flow mapping with μDDPIV. *Exp Fluids*, *42*, 589–599. Retrieved from https://doi.org/10.1007/s00348-007-0267-5 doi: 10.1007/s00348-007-0267-5

Schanz, D., Gesemann, S., & Schröder, A. (2016). Shake-The-Box: Lagrangian particle tracking at high particle image densities. *Experiments in Fluids*, *57*(5), 70. Retrieved from http://dx.doi.org/10.1007/s00348-016-2157-1 doi: 10.1007/s00348-016-2157-1

Schlatter, P., & Örlü, R. (2010a). Assessment of direct numerical simulation data of turbulent boundary layers. *Journal of Fluid Mechanics*, *659*, 116–126. doi: 10.1017/S0022112010003113

Schlatter, P., & Örlü, R. (2010b). Assessment of direct numerical simulation data of turbulent boundary layers. *Journal of Fluid Mechanics*, *659*, 116–126. Retrieved from https://doi.org/10.1017/S0022112010003113 (Publisher: Cambridge University Press) doi: 10.1017/S0022112010003113

Schröder, G., & Treiber, H. (2002). *Technische Optik: Grundlagen und Anwendungen*. Vogel.

Sheng, J., Malkiel, E., & Katz, J. (2008). Using digital holographic microscopy for simultaneous measurements of 3d near wall velocity and wall shear stress in a turbulent boundary layer. *Experiments in Fluids*, *45*(6), 1023–1035. Retrieved from 10.1007/s00348-008-0524-2 doi: 10.1007/s00348-008-0524-2

Sillero, J. A., Jiménez, J., & Moser, R. D. (2013). One-point statistics for turbulent wall-bounded flows at reynolds numbers up to $\delta^+ \approx 2000$. *Physics of Fluids*, *25*(10). (Publisher: AIP Publishing) doi: 10.1063/1.4823831

Simens, M. P., Jiménez, J., Hoyas, S., & Mizuno, Y. (2009). A high-resolution code for turbulent boundary layers. *Journal of Computational Physics*, *228*(11), 4218–4231. Retrieved from https://doi.org/10.1016/j.jcp.2009.02.031 doi: 10.1016/j.jcp.2009.02.031

Virtanen, P., Gommers, R., Oliphant, T. E., Haberland, M., Reddy, T., Cournapeau, D., … SciPy 1.0 Contributors (2020). SciPy 1.0: Fundamental Algorithms for Scientific Computing in Python. *Nature Methods*, *17*, 261–272. doi: 10.1038/s41592-019-0686-2

Willert, & Klinner, J. (2024). Dynamic wall shear stress measurement using event-based 3d particle tracking. In *21st international symposium on application of laser and imaging techniques to fluid mechanics.* Lisbon, Portugal. Retrieved from https://elib.dlr.de/204677/

Willert, C. (2015). High-speed particle image velocimetry for the efficient measurement of turbulence statistics. *Experiments in Fluids*, *56*(1), 17. Retrieved from http://link.springer.com/10.1007/s00348-014-1892-4 doi: 10.1007/s00348-014-1892-4

Willert, C., & Gharib, M. (1992). Three-dimensional particle imaging with a single camera. *Experiments in Fluids*, *12*(6), 353–358. Retrieved from https://link.springer.com/article/10.1007/BF00193880 doi: 10.1007/BF00193880

Willert, C., Novara, M., Schanz, D., Geisler, R., Schroll, M., Ribergard, S., & Schröder, A. (2021). Multi-resolution, time-resolved PIV measurements of a Decelerating Turbulent Boundary Layer near Separation. *14th International Symposium on Particle Image Velocimetry*, *1*(1). Retrieved from https://ispiv21.library.iit.edu/index.php/ISPIV/article/view/77 doi: 10.18409/ispiv.v1i1.77

Willert, C. E., Cuvier, C., Foucaut, J. M., Klinner, J., Stanislas, M., Laval, J. P., ... Röse, A. (2018). Experimental evidence of near-wall reverse flow events in a zero pressure gradient turbulent boundary layer. *Experimental Thermal and Fluid Science*, *91*, 320–328. Retrieved from https://www.sciencedirect.com/science/article/pii/S0894177717303394 doi: 10.1016/j.expthermflusci.2017.10.033

Yoon, S. Y., & Kim, K. C. (2006). 3d particle position and 3d velocity field measurement in a microvolume via the defocusing concept. *Measurement Science and Technology*, *17*(11), 2897–2905. doi: 10.1088/0957-0233/17/11/006

Örlü, R., & Vinuesa, R. (2020). Instantaneous wall-shear-stress measurements: advances and application to near-wall extreme events. *Measurement Science and Technology*, *31*(11), 112001. (Publisher: IOP Publishing) doi: 10.1088/1361-6501/aba06f